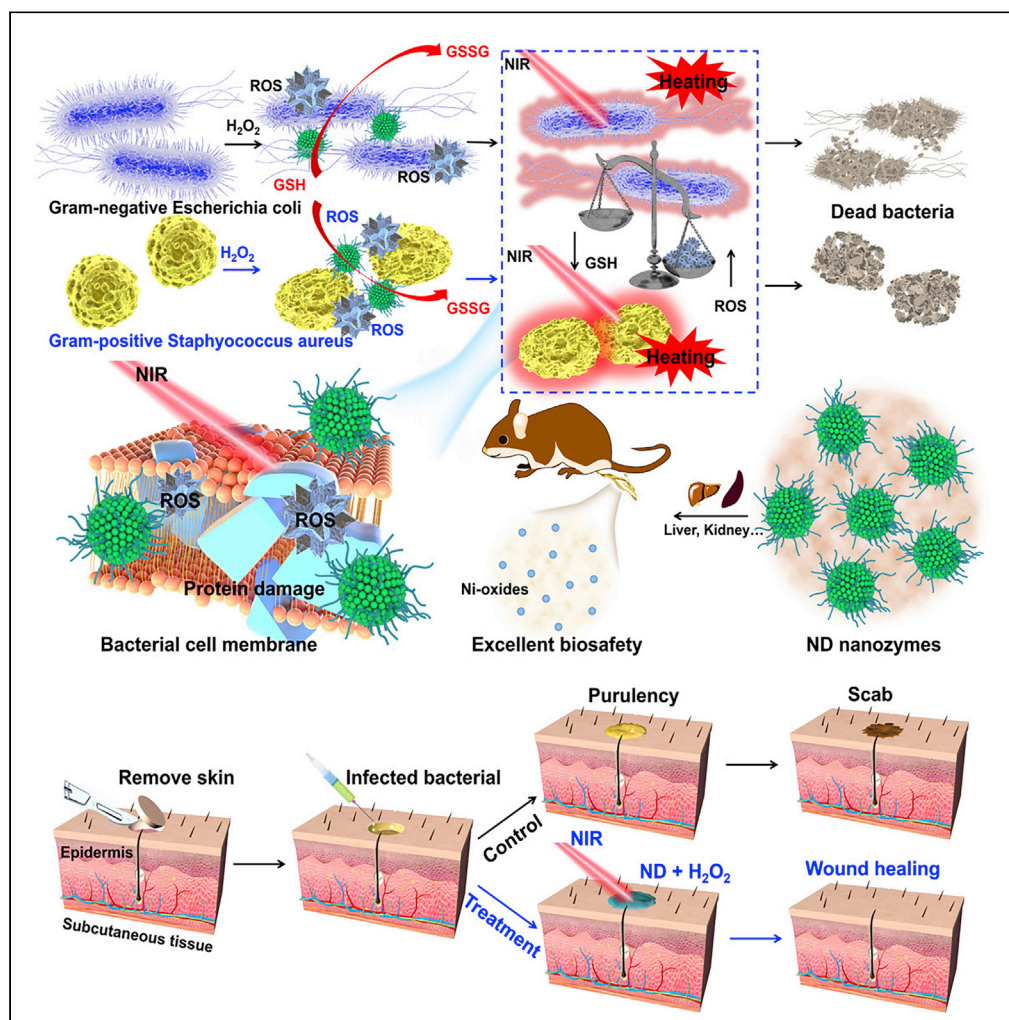**Article**

Biodegradable Nickel Disulfide Nanozymes with GSH-Depleting Function for High-Efficiency Photothermal-Catalytic Antibacterial Therapy

Xianwen Wang, Linxin Fan, Liang Cheng, ..., Yan Ma, Zhaohua Miao, Zhengbao Zha

lcheng2@suda.edu.cn (L.C.)
zbzha@hfut.edu.cn (Z.Z.)

HIGHLIGHTS

ND nanozymes have good photothermal and catalysis effect and GSH-depleting function

The multifunctional ND nanozymes have achieved satisfactory antibacterial effects

The biodegradable ND nanozymes have a wide application in precise sterilization

Article

Biodegradable Nickel Disulfide Nanozymes with GSH-Depleting Function for High-Efficiency Photothermal-Catalytic Antibacterial Therapy

Xianwen Wang,[1,2] Linxin Fan,[1] Liang Cheng,[2,4,*] Yanbin Sun,[1] Xiyu Wang,[2] Xiaoyan Zhong,[3] Qianqian Shi,[1] Fei Gong,[2] Yu Yang,[2] Yan Ma,[1] Zhaohua Miao,[1] and Zhengbao Zha[1,*]

SUMMARY

Bacterial infections caused by pathogens have always been a thorny issue that threatens human health, and there is urgent need to develop a new generation of antimicrobial nano-agents and treatments. Herein, biodegradable nickel disulfide (ND) nanozymes as excellent antibacterial agents that integrate excellent photothermal performance, nano-catalysis property, and glutathione (GSH)-depleting function have been successfully constructed. The ND nanozymes can effectively catalyze the decomposition of H_2O_2 to produce $\cdot OH$, and the hyperthermia of ND nanozymes generated by photothermal therapy (PTT) can further increase its catalytic activity, which provides rapid and effective bacterial killing effect compared with nano-catalytic treatment or PTT alone. Surprisingly, the ND nanozymes have the ability of GSH consumption, thus enhancing its sterilization effect. Moreover, the ND nanozymes are biodegradable nanomaterials that do not cause any significant toxicity *in vivo*. Collectively, the ND nanozymes with excellent photothermal performance, catalytic activity, and GSH-depleting function are used for high-efficiency sterilization.

INTRODUCTION

Bacterial infection has become a fatal worldwide health problem faced by human beings due to its high morbidity and mortality (Huo et al., 2019; Miao et al., 2019; Wang et al., 2019a; Wentao et al., 2019; Zhang et al., 2019b). The traditional methods to fight against bacterial infection are mainly based on antibiotics, metal ions, and quaternary ammonium ions, which are costly, toxic, and environmentally unfriendly, limiting their further use and conversion (Gao et al., 2018; Liu et al., 2020; Zhang et al., 2019a). Moreover, the excessive use of antibiotics leads to the generation of bacterial resistance, the treatment effect is inevitably reduced and even leads to the production of super-bacteria, thus causing a major threat to people's health and safety (Huo et al., 2019). Thus, it is of great significance to explore a new therapeutic strategy to more effectively and safely fight bacterial infections without having obvious side effects and resulting drug resistance (Liu et al., 2019b; Wang et al., 2019a).

Benefiting from the rapid rise and development of nanozymes, more attention has been paid to the study of using inorganic Fenton/Fenton-like reagents with horseradish peroxidase (HRP)-mimic ability to kill bacteria (Cao et al., 2019; Sang et al., 2019; Xi et al., 2019a). These reagents have been generally considered explored as excellent reactive HRP-like nanozymes, which can effectively catalyze the typical peroxidase-like reaction in the presence of H_2O_2, producing lots of reactive oxygen species (ROS) that have prominent oxidation effect (e.g., $\cdot OH$) (Huo et al., 2019; Wang et al., 2020a). These HRP-like nanozymes can be delivered to and accumulated at the pathological site through the drug delivery nanoplatforms, generating a large amount of ROS, which eventually leads to the dominant inhibition and destruction of drug-resistant bacterial cells (Huo et al., 2019). Unfortunately, HRP-like nanozymes limit their further application in antimicrobials for the following several reasons. (1) Most of the reported HRP-like nanozymes are non-degradable and cannot be removed from the body after sterilization, thus inevitably causing long-term toxicity *in vivo* (Zhang et al., 2019a). (2) Glutathione (GSH) is a tripeptide molecule that widely existed in bacteria, which played an important role in the antioxidant defense system of bacteria and effectively prevented oxidative stress from damaging cell components. Thus, GSH existing in bacteria can significantly weaken the bactericidal effect of peroxide-like nanomaterials (Yan et al., 2013). (3) As previously reported, it is difficult to

[1]School of Food and Biological Engineering, Hefei University of Technology, Hefei 230009, P. R. China

[2]Institute of Functional Nano & Soft Materials (FUNSOM), Jiangsu Key Laboratory for Carbon-based Functional Materials and Devices, Soochow University, Suzhou 215123, P. R. China

[3]National Engineering Research Centre for Nanomedicine, College of Life Science and Technology, Huazhong University of Science and Technology, Wuhan 430074, P. R. China

[4]Lead Contact

*Correspondence:
lcheng2@suda.edu.cn (L.C.),
zbzha@hfut.edu.cn (Z.Z.)
https://doi.org/10.1016/j.isci.2020.101281

completely eliminate bacteria by using HRP-like nanozymes alone (Liu et al., 2019b; Qing et al., 2019). The combination therapy based on sterilization is an effective strategy to improve the antibacterial efficiency owing to their effective synergistic effect (Liu et al., 2019c; Wu et al., 2019; Yang et al., 2019c). Hence, it is of great significance to develop biodegradable HRP-like nanozymes with multiple antibacterial function.

From the basic principle that increasing temperature can accelerate the chemical reaction rate, it is an effective strategy to improve the catalytic rate of HRP-like nanozymes by raising the temperature of bacterial infection site (Tang et al., 2017; Wang et al., 2019b, 2020b; Yang et al., 2019a). Among all the strategies currently reported for hyperthermia, photothermal therapy (PTT) is a new type of bactericidal therapy that employs photothermal agents (PTAs) to convert near-infrared light into overheating to destroy different types of pathogens and microorganisms, which is considered as one of the most promising treatment methods due to its less-invasive nature and high selectivity (Liu et al., 2019a). Therefore, developing novel HRP-like nanozymes with excellent photothermal properties will be a feasible strategy to improve the killing efficiency against bacteria (Xi et al., 2019b). To date, different HRP-like nanozymes including MoS_2 (Yin et al., 2016) nanomaterials, $CuFe_2O_4$ (Liu et al., 2019b) nanoparticles, single-iron-atom nanocatalysts (Huo et al., 2019; Xu et al., 2019), Fe_3O_4 nanomaterials (Xu et al., 2018), carbon nanoparticles (Xi et al., 2019b), etc., have been reported for photothermal-catalytic antimicrobial therapy. However, the non-biodegradability of HRP-like nanozymes would lead to long-term toxicity in vivo (Yang et al., 2019b). More importantly, all these nanozymes have no GSH depletion function, which weakens their antibacterial effect. Based on this, the development of biodegradable HRP-like nanozymes with GSH-depleting function for photothermal-catalytic antimicrobial therapy is challenging and meaningful.

Nickel-based nanomaterials have been widely used in the field of nanomedicine owing to their good biocompatibility, prominent photothermal performance, and biodegradability (Liu et al., 2019d; Wang et al., 2017). It is worth noting that nickel-based nanomaterials are an excellent HRP-like nanozyme that can detect H_2O_2 and glucose by colorimetry (Chen et al., 2018; He et al., 2019). However, their peroxides-like catalytic activity and photothermal properties have not been reported for sterilization. Inspired by the outstanding peroxide activity and the photothermal properties of nickel-based nanomaterials, it is speculated that the combination of HRP-like catalytic activity and PTT may make up for the deficiency of single-mode antibacterial strategy and improve the antibacterial performance of the wound. Herein, monodisperse nickel disulfide (ND) nanozymes were fabricated through a facile solvothermal process, the as-prepared ND nanozymes had satisfactory near-infrared (NIR) absorption, high photothermal conversion efficiency, and excellent peroxide-like catalytic activity (Scheme 1A). The obtained ND nanozymes could generate ·OH through Fenton-like reaction in the presence of H_2O_2, and the catalytic activity of ND nanozymes was further enhanced by the mild photothermal performance, which has led to the achievement of photothermally enhanced catalytic bacterial treatment in vitro. Surprisingly, the ND nanoparticles could also act as another kind of enzyme (glutathione peroxidase mimetic, GSH-P_x) that accelerated the consumption of GSH by oxidizing molecules and further weakened the bacteria through the GSH removal ability of ROS, thus enhancing its sterilization effect. More importantly, the experimental results of wound healing showed that the synergetic antibacterial nanoplatform could be easily used for wound disinfection (Scheme 1B). Most importantly, the ND nanozymes could quickly be removed from the body through urine and feces, due to the property of rapid biodegradability, without causing any significant toxicity through the systematic evaluation. Overall, the biodegradable ND nanozymes as multifunctional antibacterial agents have a broad prospect for accurate antibacterial application.

RESULTS

Characterization of ND Nanozymes

Monodisperse and uniform ND nanozymes were successfully prepared by a facile PVP-assisted solvothermal method (Figure 1A), and the formation mechanism could be explained by the La Mer scheme based on the previous report (Wang et al., 2020b). Transmission electron microscopic (TEM) images of as-prepared ND nanozymes clearly revealed a uniform spherical morphology with an average diameter of 112.31 ± 24.07 nm (Figures 1B, 1C, and 1E). In addition, the TEM image further demonstrated that the ND nanozymes had highly ordered pore structures, which was due to the spherical accumulation of NiS_2 nanocrystals (Figure 1C). High-resolution TEM image showed that the lattice spacing was measured to be ~0.198 nm, corresponding to the (220) interplanar spacing of the cubic ND (Figure 1D). The diffraction rings of selected area electron diffraction (SAED) image indicated that the synthesized ND nanozymes had polycrystalline structure (Figure S1). The crystal structure and purity of the samples were also determined by X-ray diffraction. All the diffraction peaks corresponded to the cubic ND crystals
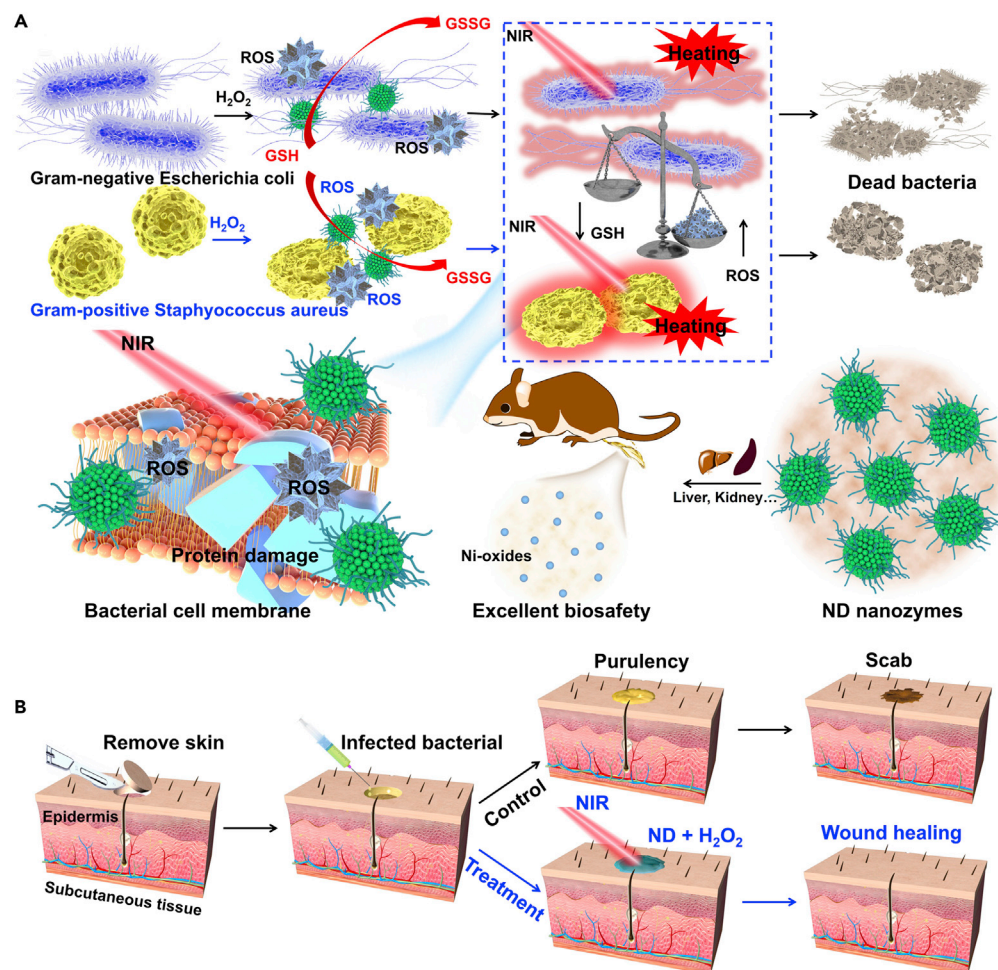
Scheme 1. Scheme of the Biodegradable ND Nanozymes with GSH-depleting Function for High-efficiency Photothermal-catalytic Antibacterial Therapy

(A) *in vitro* and (B) *in vivo*.

(JCPDS No. 65-3325), suggesting the good crystallinity and purity of the synthesized ND nanozymes (Figure 1F). The mole ratio of Ni and S elements in ND was close to 1: 2, proved by energy-dispersive X-ray spectroscopic spectrum and the inductively coupled plasma optical emission spectroscopy (Figure 1F). In addition, field emission scanning transmission electron microscopic elemental mapping proved that the ND nanozymes were uniformly composed of Ni and S elements (Figure 1G). Moreover, X-ray photoelectron spectroscopy (XPS) was used to further confirm the chemical composition and the surface elemental states of ND nanozymes (Figures 1H–1J). The Ni, S, and O, C, and N elements existed in the full-scan XPS survey spectrum of ND nanozymes, where C, N, and O elements mainly come from the substrate (Figure 1I). In the Ni 2p spectra (Figure 1J), the peaks located at 871.49 and 853.85 eV correspond to Ni $2p_{1/2}$ and Ni $2p_{3/2}$ of the Ni^{2+} ions, respectively, along with two satellite peaks at about 874.90 and 859.22 eV. In the S 2p spectra (Figure 1K), the binding energies of S $2p_{1/2}$ and S $2p_{3/2}$ were clearly observed at about 162.44 and 163.67 eV of S elements, showing the presence of S-S bonds in the ND nanozymes (He et al., 2019). Besides, the peaks located at 168.41 eV were attributed to S-O bonds, which were caused by the surface oxidation of ND nanozymes. In addition, the zeta potential of the ND nanozymes was measured to be -9.80 ± 0.12 mV. All the aforementioned results demonstrated that ND nanozymes with high purity and quality were successfully prepared through a simple solvothermal method.

Photothermal Performance of ND Nanozymes

Good NIR absorbance and excellent photothermal conversion efficiency are the two most basic prerequisites of PTAs (Wang et al., 2017). Excitingly, the synthesized ND nanozymes exhibited wide NIR
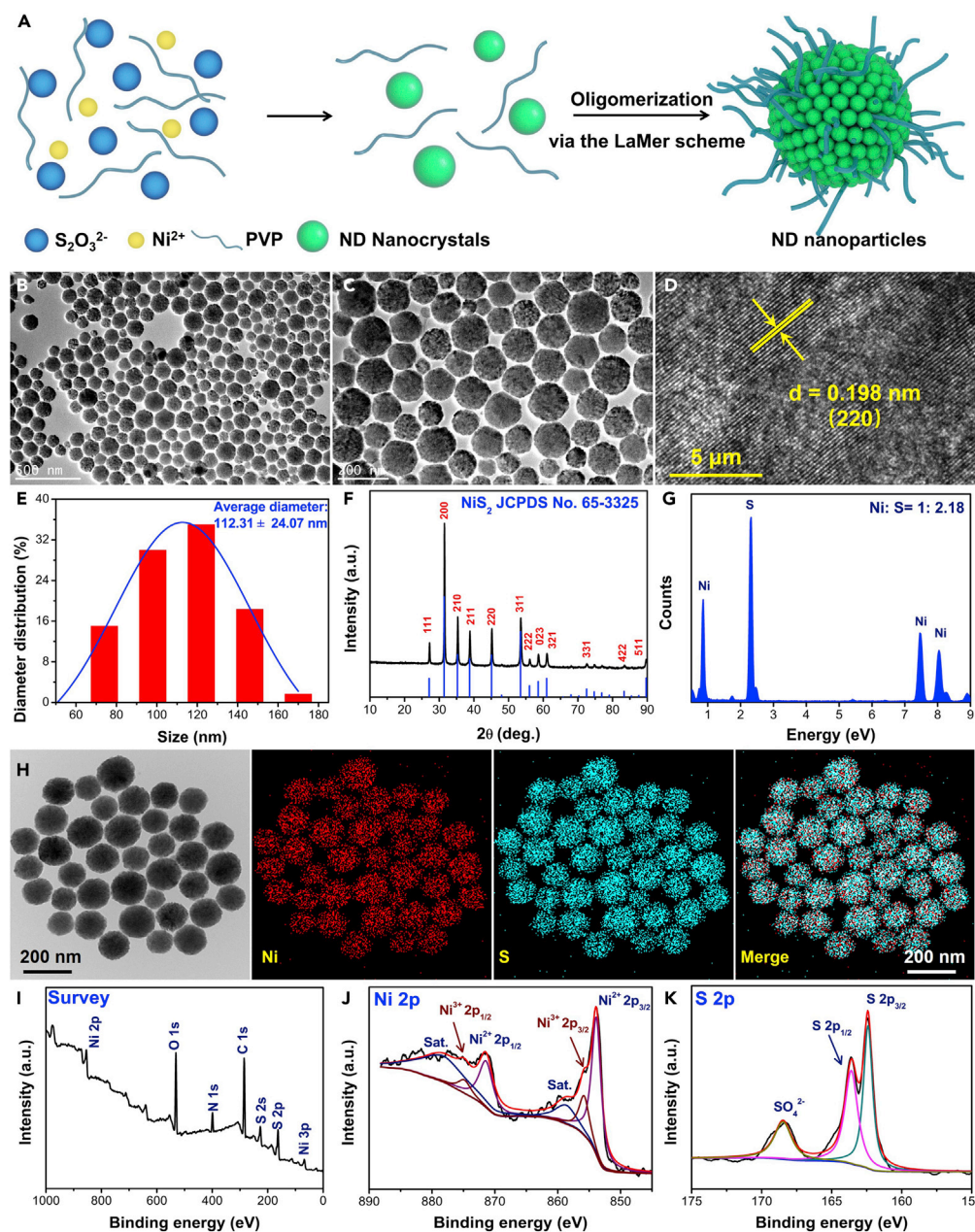
Figure 1. Characterization of the As-prepared ND Nanozymes

(A–H) (A) Preparation scheme of ND nanoparticles, (B and C) TEM images, (D) high-resolution TEM image of ND nanozymes, (E) the size distribution determined from (B), (F) X-ray diffraction pattern, (G) energy-dispersive X-ray spectrum, and (H) scanning transmission electron microscopic elemental mapping (Ni, S, merge) of the ND nanozymes. (I–K) XPS characterization of ND nanozymes. The survey spectra (I) and the core level spectra of (J) Ni 2p and (K) S 2p. See also Figure S1.

absorbance, which increased linearly with the enhancing concentration of ND nanozymes (Figure 2A). In addition, the mass extinction coefficient of ND nanozymes was $\sim$22.46 L g^{-1} cm^{-1} (Figure S2), much higher than those of most reported PTAs (Zhang et al., 2016), suggesting that ND nanozymes could be used as ideal PTAs for photothermal sterilization. To study the photothermal performance, the ND nanozymes with gradient concentrations were irradiated by the NIR laser (808 nm, 0.75 W/cm^2) for 10 min (Figure 2B). Particularly, when the concentration of ND nanozymes was $\sim$75 μg/mL, the temperature could be increased from 28 to 51.4 °C, whereas the temperature of pure water only increased by 1.6 °C under the same
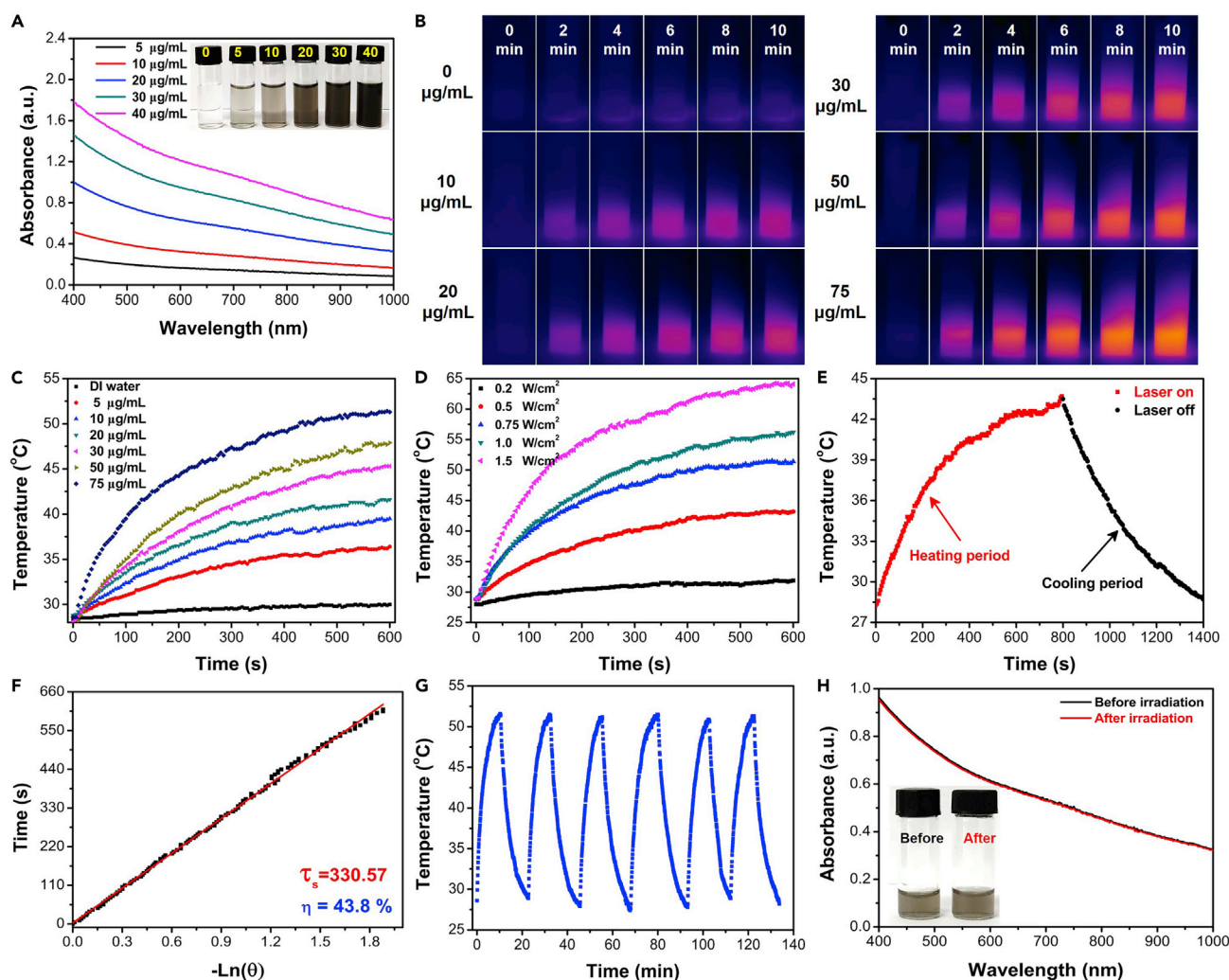
Figure 2. The Photothermal Effect of the As-prepared ND Nanozymes

(A–C) (A) UV-vis-NIR spectra (insets: photographs of NPs with different concentrations), (B) NIR thermal images, and (C) the corresponding temperature change curves of ND nanozymes with gradient concentrations under NIR irradiation (808 nm, 0.75 W/cm^2, 10 min).

(D) Temperature heating curves under NIR irradiation with various power densities (ND nanozymes: 75 μg/mL, 808 nm, 10 min).

(E) The temperature profile of ND nanozymes (20 μg/mL) irradiated by NIR laser (808 nm, 0.75 W/cm^2) for 12 min, followed by natural cooling to room temperature.

(F) The time constant was determined to be τ_s = 330.57 s, and photothermal conversion efficiency of ND nanozymes was as high as ~43.8%.

(G and H) (G) The photothermal stability (six laser on/off cycles) and (H) UV-vis-NIR spectra and photographs of the ND nanozymes before and after six laser on/off cycles.

See also Figures S2–S7 and Table S1.

condition (Figure 2C). The photothermal effect of ND nanozymes exhibited an irradiation time-dependent, concentration-dependent, and power density-dependent elevation, like that of most reported PTAs (Figures 2D and S3–S6). The photothermal conversion efficiency of ND nanozymes was measured to be ~43.8% based on the previously reported method (Figures 2E and 2F) (Wang et al., 2019b), which was comparable to those of many reported PTAs (Table S1) (Yong et al., 2014). In addition, the photothermal stability of ND nanozymes was explored by six laser irradiation cycles, the amplitude of temperature elevation, the UV-visible-NIR (UV-vis-NIR) absorption spectrum, and the color of ND nanozyme solution were not significantly changed before and after cycling laser irradiation (Figures 2G, 2H, and S7), suggesting that the as-obtained ND nanozymes possessed satisfactory photothermal stability. Hence, the prominent photothermal performance of ND nanozymes suggested that they could be used as potential PTAs for photothermal sterilization.

Catalytic Properties and GSH-Depleting Functions of ND Nanozymes

Nickel-based compounds are ideal catalysts with the properties of HRP-like enzyme, which have been reported for the detection of H_2O_2 and glucose. However, their catalytic properties have not been reported in the field of nanomedicine. The excellent catalytic activity of nickel-based compounds makes them have broad application prospects in sterilization. The HRP-like catalytic properties of the synthesized ND nanozymes were evaluated through the catalytic oxidation of 3,3′,5,5′-tetramethylbenzidine (TMB), one of the most widely used indicators of •OH, which would be gradually changed from colorless to blue. In the presence of H_2O_2, the ND nanozymes changed the color of TMB probe from colorless to dark blue, whereas the control group showed no color change (Figure 3A). With the increase of H_2O_2 concentration, the color of the solution became bluer (Figure 3B), indicating that the catalytic activity of the ND nanozymes depended on the concentration of H_2O_2. Besides, o-phenylenediamine (OPDA) probe was further used to check the catalytic properties of ND nanozymes. Similar phenomena and results were observed by using the OPDA probe (Figures 3C–3E), which indicated that the ND nanozymes have excellent HRP-like enzyme catalytic properties. The Michaelis-Menten constant (K_m) and maximum velocity (V_{max}) of ND nanozymes were calculated by TMB detection, which were calculated to be ∼3.64 mM and ∼1.55×10^{-4} mM min^{-1}, respectively (Figure S8). This relatively low Km value indicated the good catalytic performance of ND nanozymes.

Some reducing substances such as glutathione (GSH) present in bacteria (0.1–10 mmol/L) can weaken ROS-induced bacterial killing. Based on this, the properties of ND nanozymes in depleting GSH were explored by using 5,5′-dithio-bis (2-nitrobenzoic acid) (DTNB) probe (Shan et al., 2019). When the molar ratio of GSH to ND nanozymes was 1: 1, the characteristic peak of DTNB at 420 nm gradually decreased with the extension of reaction time (Figure 3F) and the GSH could be completely consumed after 1.0-h incubation, indicating that the ND nanozymes had a remarkable GSH consumption ability (Figure 3G). The clearance rate of GSH was ∼16.27%, 32.24%, 68.51%, 83.47%, 90.60%, and 99.58% at 5, 10, 20, 30, 40, and 60 min, respectively. When the molar ratio of GSH to ND nanozymes was increased to 10: 1, GSH still was completely consumed, but the rate of GSH consumption became slower (Figures 3H and 3I), indicating that the ability of ND nanozymes to consume GSH exhibited dose-dependent performance. The clearance rate of GSH was ∼15.03%, 35.10%, 54.83%, 67.15%, 82.36%, and 99.66% at 1, 2, 3, 4, 6, and 10 h, respectively. As the concentration of GSH was much higher than that of ND nanozymes, the ability of ND nanozymes to consume GSH could not be explained by redox. It was more likely that the ND nanozymes acted as GSH-like mimetic enzymes based on previous reports, resulting in extraordinary GSH-depleting function of ND nanozymes (Zhong et al., 2020).

In Vitro Antibacterial Performance of ND Nanozymes

Based on the excellent properties including photothermal effect, GSH-depleting function, and catalytic performance, it is speculated that the ND nanozymes could act as potential therapeutic agents for the treatment of bacterial infection by photothermal and catalytic properties. Therefore, the *in vitro* synergistic antibacterial effect of the ND nanozymes against *Escherichia coli* (*E. coli*, DH5α) and methicillin-resistant *Staphylococcus aureus* (MRSA, Mu50) was systematically evaluated. As for killing *E. coli*, lots of viable colonies formed on LB agar plates in the groups of control and NIR, suggesting that NIR irradiation alone did not affect *E. coli* growth. The antibacterial effect of the groups of H_2O_2 and H_2O_2 + NIR was weak, which was caused by the poor bactericidal effect of the limited H_2O_2. Interestingly, the pure ND nanozymes themselves also had some antibacterial effect, which may be due to their ability to attach on the surface of bacteria, resulting in the death of some bacteria. In the group of ND nanozymes + H_2O_2, the more obvious antibacterial efficiency was observed compared with the groups of H_2O_2 and ND nanozymes, with the bacterial survival rate of ∼16.87%. These data demonstrated that the ND nanozymes could catalyze the degradation of H_2O_2 by Fenton-like reaction and produce more toxic •OH, which further enhanced the bactericidal effect. In the group of ND nanozymes + NIR, the survival rate of bacteria was only ∼1.67%, suggesting that the photothermal antibacterial effect of ND nanozymes had good results. In the group ND nanozymes + H_2O_2 + NIR, the bacteria had completely died, and the inhibition rate was ∼100% (Figures 4A and 4C). Similarly, as for killing MRSA, the corresponding treatment groups showed the same antibacterial trend as *E. coli* (Figures 4B and 4E). All these data together demonstrated that the photothermal-catalytic antibacterial effect of ND nanozymes had achieved more obvious sterilization efficiency.

To further clearly evaluate the antibacterial effect of ND nanozymes, the bacterial samples (*E. coli* and MRSA) after different treatments were immediately stained with SYTO 9 (viable bacteria, green fluorescence) and propidium iodide (dead bacteria, red fluorescence) for 30 min, respectively, and then were
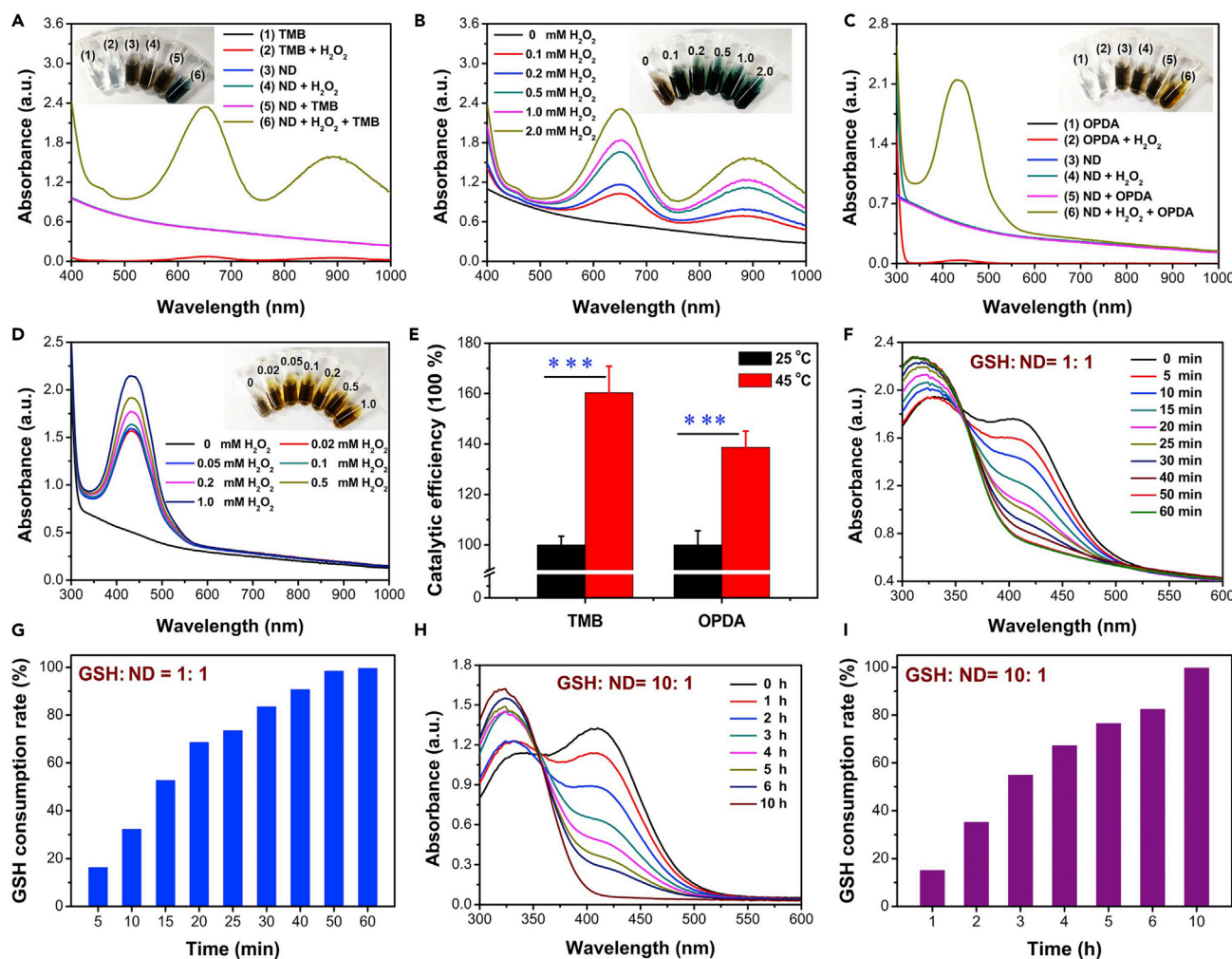
Figure 3. Catalytic Properties and GSH-Depleting Functions of ND Nanozymes

(A and B) (A) The peroxidase-like catalytic effect of ND nanozymes at different conditions and (B) at various H_2O_2 concentrations by using the TMB probe.

(C and D) (C) The peroxidase-like catalytic effect of ND nanozymes at different conditions and (D) at various H_2O_2 concentrations by using the OPDA probe.

(E) Effect of temperature on its catalytic activity.

(F and G) (F) Time-dependent GSH depletion and (G) GSH consumption rate by ND nanozymes (the mole ratio of GSH and ND nanozymes is 1: 1).

(H and I) (H) Time-dependent GSH depletion and (I) GSH consumption rate by ND nanozymes (the mole ratio of GSH and ND nanozymes is 10: 1).

See also Figure S8.

observed with a fluorescence microscope. In the control, NIR, H_2O_2, H_2O_2 + NIR, and ND nanozymes groups, only negligible red fluorescence was observed in *E. coli* and MRSA. However, a large amount of red fluorescence was observed in the ND nanozymes + H_2O_2 group, indicating that the •OH generated by the Fenton-like reaction could significantly increase the antibacterial effect. In addition, a large amount of red fluorescence was observed in the ND nanozymes + NIR group, whereas only red fluorescence was found in the ND nanozymes + H_2O_2 + NIR group (Figures 4D and 4F). These results indicated that the combination of photothermal performance and catalytic properties of ND nanozymes could significantly improve its bactericidal efficiency.

From the aforementioned study, the ND nanozymes achieved good bactericidal effect *in vitro*, and then we further evaluated its antibacterial mechanism. Scanning electron microscopy (SEM) was used to elucidate the antibacterial effect by observing the morphological changes of bacteria from different groups (Figures 5A and 5B). The surfaces of bacteria (*E. coli* and MRSA) were intact and smooth in the control group, similarly, the bacteria in the NIR, H_2O_2, H_2O_2 + NIR, and ND nanozymes groups also showed negligible
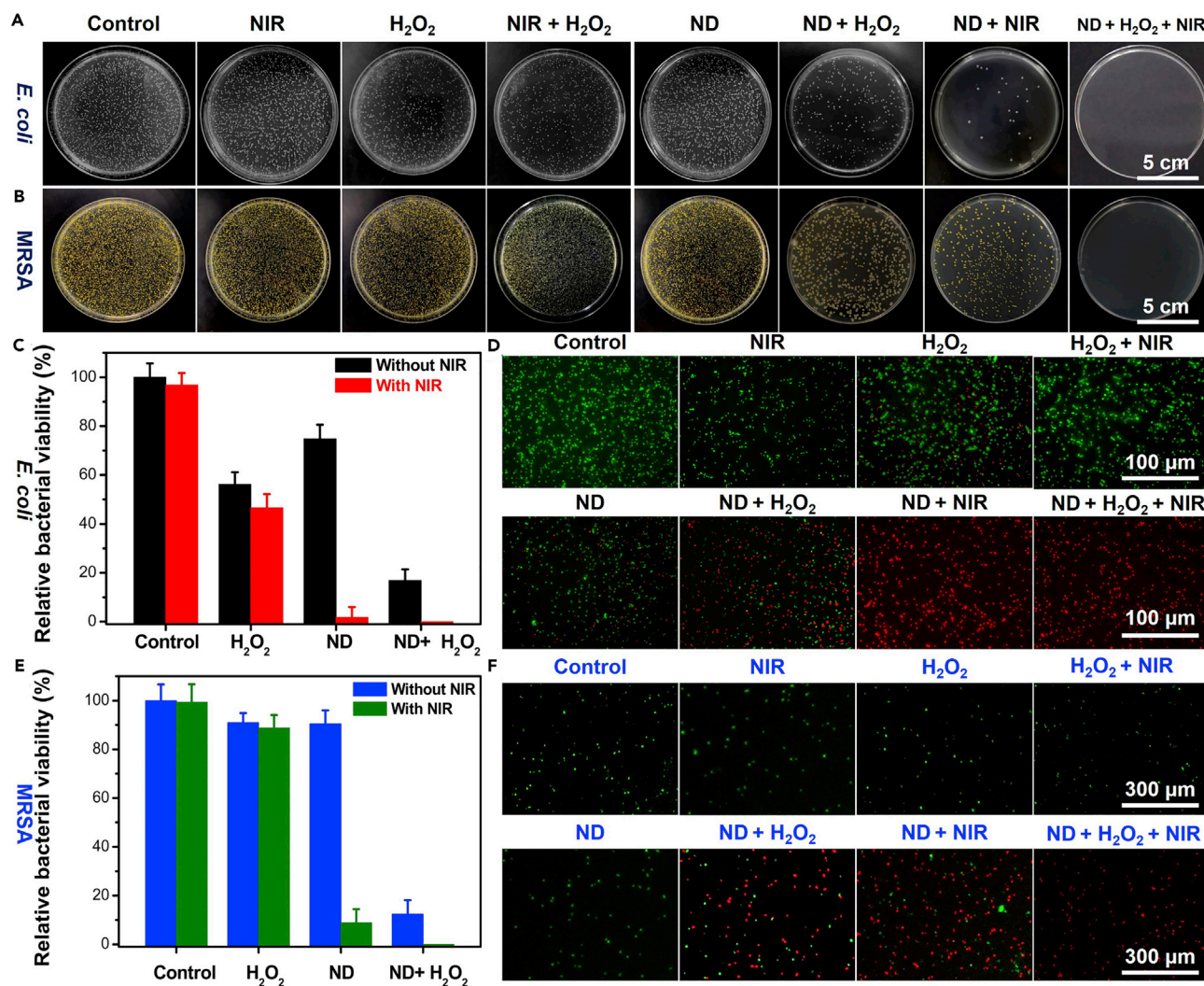
Figure 4. *In Vitro* Antibacterial Performance of the ND Nanozymes
(A–F) Photographs of the bacterial colonies formed by (A) *E. coli* and (B) MRSA after different treatments. (C and E) Survival rates corresponding to (A) and (B). Fluorescent images of (D) *E. coli* and (F) MRSA stained with propidium iodide and SYTO 9 after different treatments.

distortion and wrinkle, indicating that these groups had little effect on the integrity of bacterial cell membrane after different treatment. On the contrary, there were obvious cell deformation and content leakage in the ND nanozymes + H_2O_2 group, which indicated that the catalytic performance of ND nanozymes caused the bacterial damage. However, the bacterial surfaces became more wrinkled and rougher in the ND nanozymes + NIR group compared with ND nanozymes + H_2O_2 group, while the bacteria completely lost their cell integrity and the matrix flowed out, which implied that the synergistic effect had a stronger antibacterial ability. Therefore, this novel antibacterial nanoagent with excellent photothermal performance and catalytic effect based on ND nanozymes could rapidly and effectively destroy *E. coli* and MRSA.

It is well known that oxidative stress plays an important role in the nanomaterials-mediated antimicrobial systems (Yin et al., 2016). The first thing that needs to be known for this antibacterial strategy is whether ROS-dependent oxidative stress will occur. First, the ROS probe, 2′,7′-dichlorodihydrofluorescein diacetate was used to detect ROS after different treatments (Wang et al., 2019b). No obvious green fluorescence was observed in the control, NIR, H_2O_2, H_2O_2 + NIR, ND nanozymes, and ND nanozymes + NIR groups, but weak green fluorescence was observed in ND nanozymes + H_2O_2 group, indicating that ND nanozymes could effectively generate •OH in the presence of H_2O_2. More importantly, the strongest green
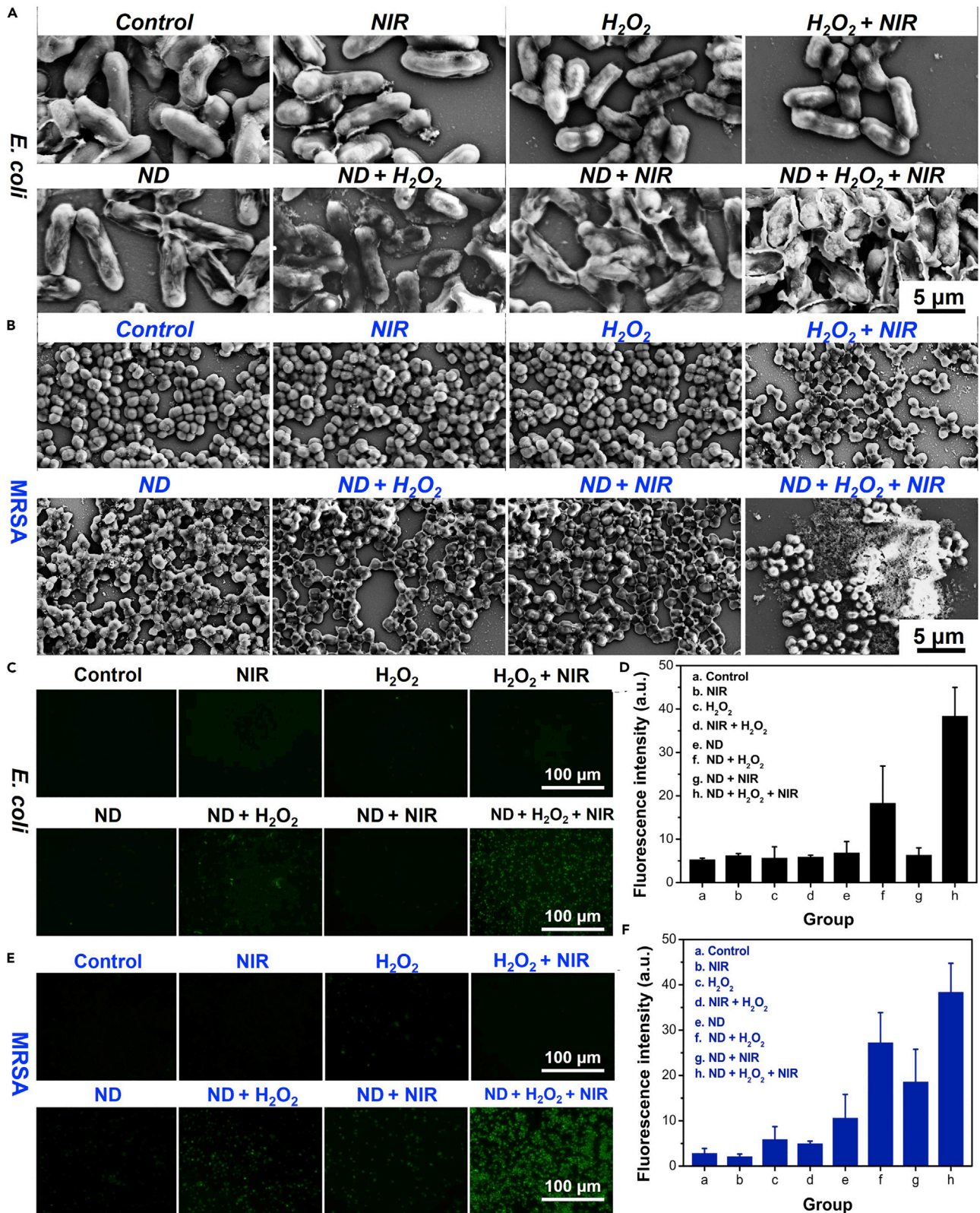
A

B

C

D

E

F

Figure 5. Antibacterial Mechanism of ND Nanozymes

(A–F) SEM images of the (A) *E. coli* and (B) MRSA samples after different treatments. The fluorescent images of (C) *E. coli* and (E) MRSA stained with 2′,7′-dichlorodihydrofluorescein diacetate after different treatments; (D) and (F) the relative fluorescence intensities corresponding to (C) and (E), respectively.

fluorescence was found in the ND nanozymes + H_2O_2 + NIR group, compared with other groups (Figures 5C–5F), indicating that the heat generated by PTT further improved the catalytic performance of ND nanozymes, thus producing more •OH and leading to better bactericidal effect.

Second, GSH is a tripeptide molecule widely existing in bacteria (0.1–10 mmol/L) that played an important role in the antioxidant defense system of bacteria and effectively prevented oxidative stress from damaging cell components (De Zoysa et al., 2008; Yan et al., 2013). Therefore, GSH level can be used as an indicator of bacterial oxidative stress, and the GSH depletion by the ND nanozymes was determined via the Ellman method. In the experiment, the fluorescence probe o-phthaldialdehyde was used to detect intracellular GSH changes. For *E. coli*, GSH could not be obviously consumed in the control (percentage of GSH consumption: 0% $\pm$ 3.64%), H_2O_2 (4.28% $\pm$ 2.66%), NIR (2.75% $\pm$ 2.55%), and H_2O_2 + NIR (9.37% $\pm$ 3.62%) groups, and it could be found that ND nanozymes (28.81% $\pm$ 4.25%) could effectively deplete GSH, further indicating that the ND nanozymes had good GSH depletion ability. GSH consumption was further improved in the ND nanozymes + H_2O_2 (46.23% $\pm$ 3.67%) and ND nanozymes + NIR (54.25% $\pm$ 4.32%) groups, whereas in the ND nanozymes + H_2O_2 + NIR (61.68% $\pm$ 3.24%) group the reduction of GSH content in bacteria was observed to be the most significant (Figures 6A and 6B). Similarly, the same experimental phenomena and results could be observed in MRSA bacteria (Figures 6C and 6D), further indicating that ND nanozymes could effectively consume GSH in bacteria, thereby breaking the balance of bacterial homeostasis and significantly improving sterilization effect.

The possible antibacterial mechanism of ND nanozymes was proposed based on the aforementioned results. (1) The •OH produced by H_2O_2 caused cell wall damage in the presence of ND nanozymes. (2) The mild photothermal performance could further enhance the catalytic activity of ND nanozymes. (3) The destructive physical interaction of bacteria with the sharp edges of ND nanozymes was enhanced due to increased component motion at high temperatures. (4) The ND nanozymes themselves could consume GSH in bacteria, which effectively disrupted the internal balance of the internal environment of bacteria, leading to its death (Figure 6E). Collectively, the different antibacterial mechanisms, namely, the inherent antibacterial capacity (ROS production and GSH consumption, etc.) and high photothermal sterilization, were the main reasons for its high antibacterial performance.

In Vivo Antibacterial Activity Assessment of ND Nanozymes

Inspired by the excellent antibacterial effects and biosafety *in vitro*, we further evaluated the antibacterial properties of ND nanozymes *in vivo* by using the MRSA-infected wound model (Figure 7A). First, female BALB/c mice were randomly divided into the following six groups (n = 5): (1) PBS, (2) H_2O_2, (3) ND nanozymes, (4) ND nanozymes + H_2O_2, (5) ND nanozymes + NIR light, and (6) ND nanozymes + H_2O_2 + NIR light (808 nm, 1.0 W/cm^2, 3 min). And MRSA, as a common pathogen of skin infection, was used to build a wound healing model. The concentrations of ND nanozymes and H_2O_2 were 50 μg/mL and 0.2 mM, respectively. The temperature of the wound was monitored by an infrared thermal camera (Figure 7B). The results showed that the temperature of the wound changed significantly under laser irradiation (808 nm, 1.0 W/cm^2, 3 min) in the ND nanozymes + NIR light and ND nanozymes + H_2O_2 + NIR light groups, but there was no significant change in the control group (Figure 7C). It should be noted that the temperature of the wound should be controlled around 45 °C to reflect the synergistic treatment effect of ND nanozymes. There was no significant difference in ND nanozymes and H_2O_2 alone compared with the control group after 4 days. In the ND nanozymes + H_2O_2, ND nanozymes + NIR light, and ND nanozymes + H_2O_2 + NIR light groups, the wounds showed remarkable healing and size reduction, and their relative wound area was reduced to ~28.65%, ~24.50%, and ~19.25%, respectively (Figures 7D and 7F). Furthermore, the antibacterial effects of different treatments *in vivo* were evaluated. Compared with the control group, the relative percentage of live bacteria in the wounds in the groups of ND nanozymes + H_2O_2 and ND nanozymes + NIR light was ~32.37% and ~19.47%, respectively. However, the relative percentage of live bacteria in the wounds was only ~3.61% in the ND nanozymes + H_2O_2 + NIR light group, which was significantly lower than those of the other five groups (Figures 7E and 7G). The results showed that the photothermal and catalytic properties of ND nanozymes alone had a good effect on sterilization, but the wound healing was the most obvious for the combination therapy, indicating that rapid and effective sterilization using the synergistic effect of catalytic treatment and PTT played an important role in the wound healing.
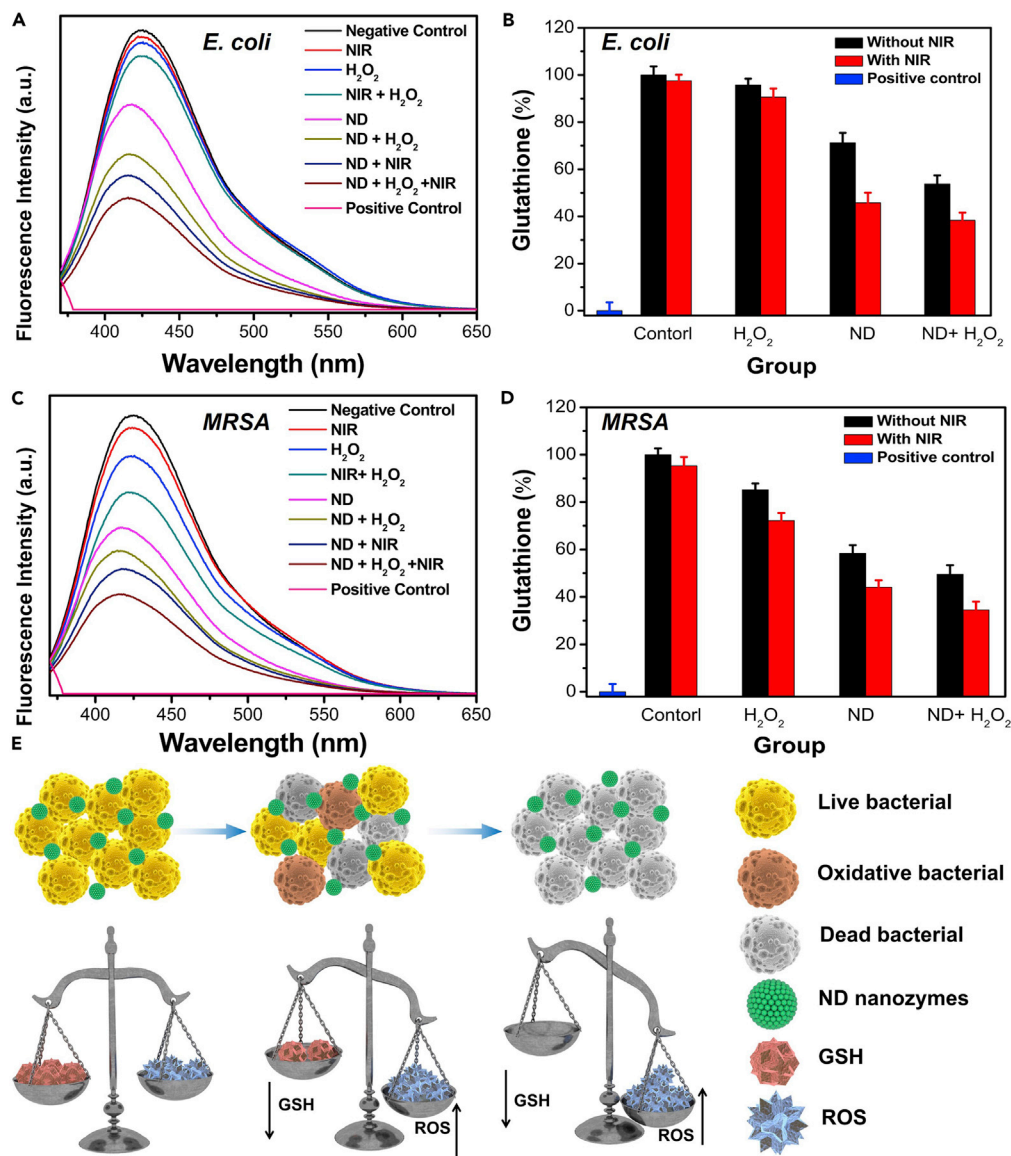
Figure 6. GSH Depletion of ND Nanozymes

(A–E) (A) Fluorescence spectra and (B) percentage of GSH depletion of *E. coli* after different treatments; (C) fluorescence spectra and (D) the percentage of GSH consumption of MRSA after different treatments; (E) schematic diagram of GSH depletion by the ND nanozymes on sterilization.

The effect of different treatments on wound healing was further evaluated by histological analysis. H&E staining showed that intact epidermal layers of wound tissue were only seen in the ND nanozymes + H_2O_2 + NIR light group, whereas more inflammatory cells were found in other five groups (Figure 7H). In addition, the presence of hair follicles in this group also indicated that the wound healed well. Furthermore, the collagen deposition of the wound tissues was evaluated by the Masson's trichrome staining. In the skin tissue treated with ND nanozymes + H_2O_2 + NIR, the collagen fibers stained blue were continuous, which was more obvious than the control group and the simple treatment group, indicating that the photothermal-catalytic combination therapy had better recovery (Figure 7I). Therefore, combined with the excellent catalytic performance and photothermal effect of ND nanozymes, effective antibacterial treatment of infectious wounds was successfully demonstrated. In addition, within the 5-day anti-infection period, there was no significant difference in body weight between mice in each group and no significant health abnormalities occurred (Figure S9). From the H&E images of the main organs of the infected or treated mice, no
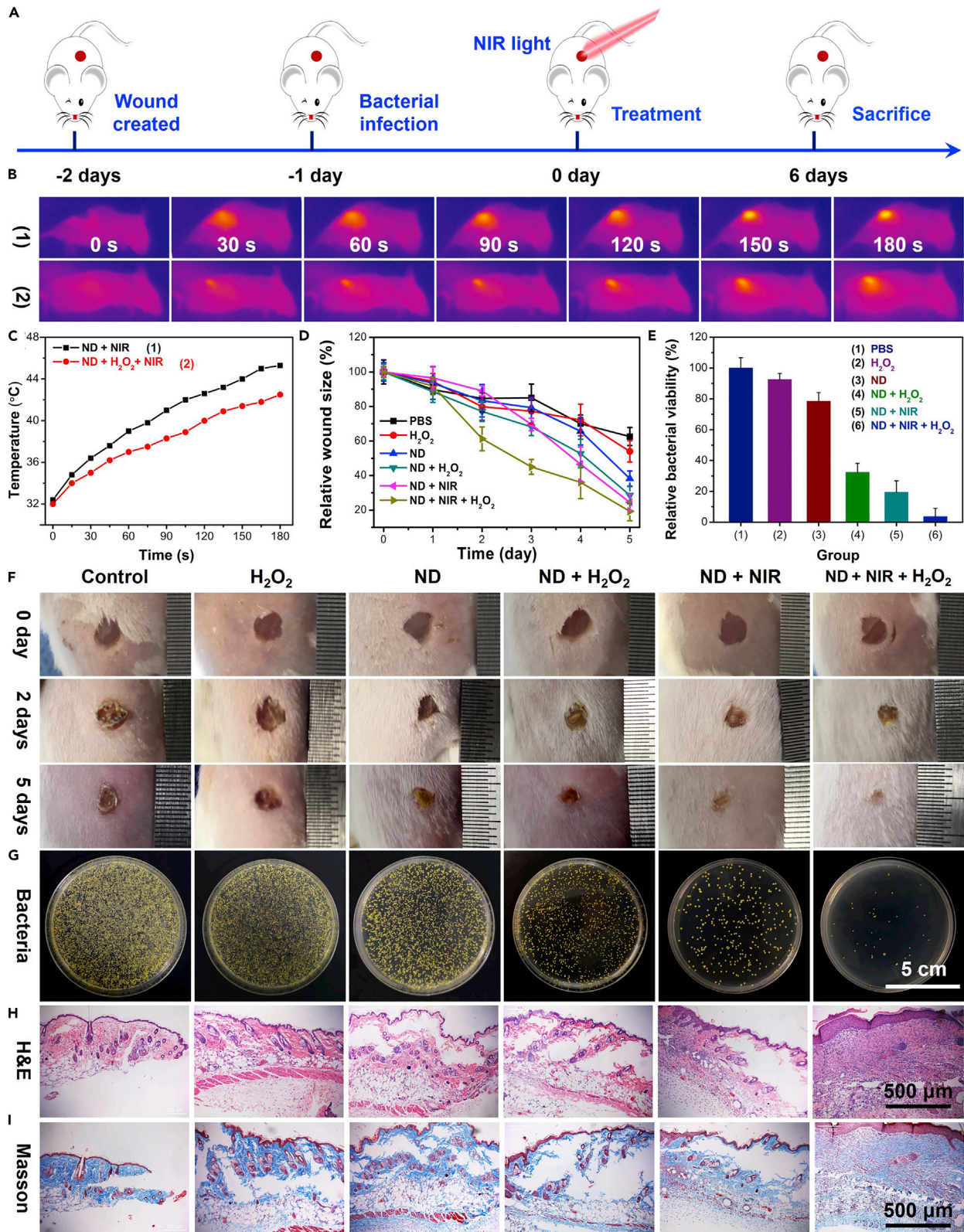
Figure 7. *In Vivo* Antibacterial Activity Assessment of the ND Nanozymes

(A–I) (A) *In vivo* antibacterial protocol in mice. (B) Infrared images and (C) temperature-elevating curves of the localized bacterial infection sites treated with ND nanozymes under NIR irradiation (808 nm, 1.0 W/cm², 2 min). (D) The relative wound size and (F) the corresponding digital photographs of mice in MRSA-infected group (n = 5). (E) The numbers of viable MRSA in infected wounds after different treatments determined by the plate counting method. (G) The photographs of bacterial colonies formed on LB agar plates from the infected wounds after different treatments. The photomicrographs of tissue sections of MRSA-infected wounds in mice after different treatments by using (H) H&E and (I) Masson staining.

See also Figures S9 and S10.

substantial pathological damage and inflammation were observed during the treatment (Figure S10), indicating that the as-prepared anti-infective ND nanozymes had outstanding biocompatibility.

Biodegradable Behavior and Biosafety Evaluation of ND Nanozymes

Biodegradable nanomaterials have higher safety than non-metabolizable nanomaterials and thus have received extensive attention in the biomedical field (Yang et al., 2019b). Many metal chalcogenides have been shown to be biodegradable nanomaterials, and it is speculated that ND nanozymes may also be a novel biodegradable nanomaterial (He et al., 2016; Wang et al., 2020b). To determine whether the synthesized ND nanozymes could be biodegraded, we carefully investigated the biodistribution and metabolic pathways of the ND nanozymes. When the ND nanozymes were intravenously (i.v.) injected into mice, the biodistribution of ND nanozymes in the main organs (heart, liver, spleen, lung, and kidney) at different time points (0, 1, 7, and 15 days) was measured. On the first day, Ni element was mainly distributed in the liver (~46.76% ID/g, the percent of injected dose per gram of tissue) and spleen (~11.55% ID/g) of the mice, the content of Ni in the main organs of mice had become very low after 15 days, and the total of liver and spleen was measured to be ~4.7% ID/g (Figure 8A), indicating that most of the ND nanozymes could be rapidly excreted from the body. It was worth noting that although ND nanozymes were gradually degraded in physiological environments and *in vivo*, however, it still showed relatively long blood circulation time after i.v. injection (Figure S11). More importantly, high concentrations of Ni element were detected in the feces and urine of mice on different days (Figure 8B), indicating that part of the ND nanozymes could be rapidly metabolized by the renal and fecal pathways.

To clarify the degradation and clearance mechanism of the synthesized ND nanozymes, a series of experiments were designed to prove our conjecture. With the prolongation of time, the UV-vis-NIR absorption of ND nanozymes aqueous solution gradually decreased, and the corresponding absorption at 808 nm was already very low on the sixth day (Figure 8C), suggesting that ND nanozymes could be rapidly degraded *in vitro*. Similar phenomena were also observed in other physiological solutions (H₂O, normal saline, PBS, PBS pH = 6.5, RPMI 1640). More importantly, the degradation rate of ND nanozymes in these physiological solutions was above ~90% on the 6th day (Figures 8D and S12). In addition, the color of ND nanozymes in these solutions gradually changed from black to colorless with extension of time (Figure 8E), which further proved that ND nanozymes could be rapidly degraded *in vitro*.

To further understand the changes in the composition and structure of ND nanozymes, the state of the sample was investigated by TEM and XPS on the fourth day. The newly prepared ND nanozymes exhibited a uniform spherical morphology, and no obvious structure was observed on the fourth day (Figure 8F). In addition, XPS was used to analyze the surface valence state change of the samples, and the characteristic peaks of Ni 2p and S 2p were significantly lower than those in the initial ND nanozymes (Figures 8G and 8H). Furthermore, obvious characteristic peaks of SO_4^{2-}, S-O bonds, O 1s were detected in the corresponding spectrum, which indicated that ND nanozymes were converted to nickel oxides (Figures 8H and 8I). Based on this, the ND nanozymes could be rapidly metabolized by the renal and fecal pathways, and the degradation mechanism of ND nanozymes could be mainly explained by the surface oxidation (Figure 8J). However, the detailed mechanism of bio-degradation needs further investigation.

Good biosafety is the primary prerequisite of nanomaterials used in the biomedical field, the biosafety of ND nanozymes was also studied in detail (Yan et al., 2019). The cytotoxicity of ND nanozymes *in vitro* was first evaluated by the typical MTT method, ND nanozymes exhibited no significant cytotoxicity even when the concentration reached 100 μg/mL (Figure S13). After i.v. injection of ND nanozymes at different time points, blood routine and blood biochemical data were collected from the mice. The parameters concerning the blood panel counts and serum biochemistry had no meaningful changes compared with the control group (Figures 9A and 9B), indicating that the ND nanozymes did not cause any significant toxicity with reasonable dose. In addition, the main organs (including heart, liver, spleen, lung, and kidney) were
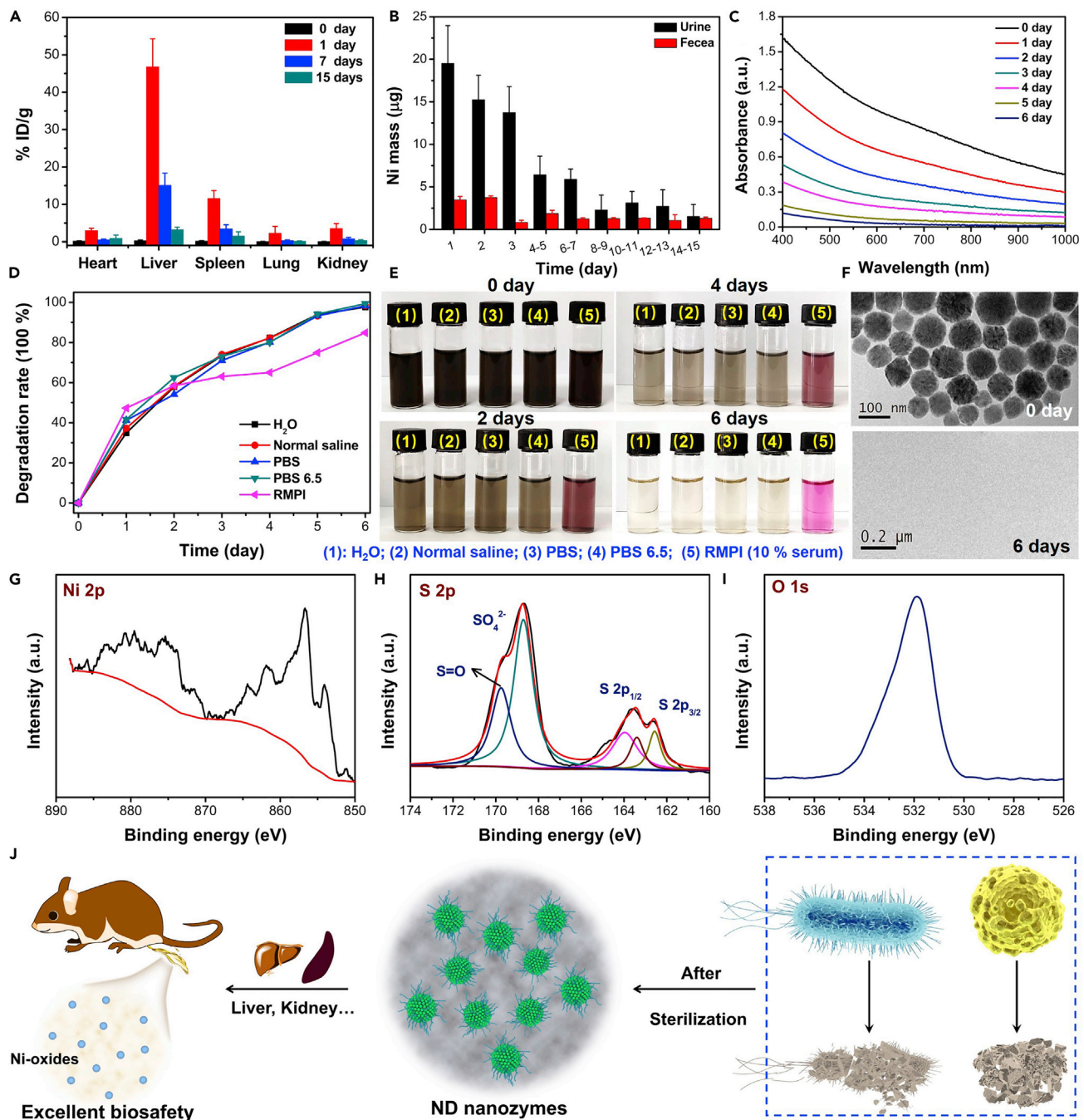
Figure 8. *In Vitro* and *In Vivo* Degradation Behavior of ND Nanozymes

(A–J) (A) Time-dependent biodistribution and (B) excretion patterns at different time points post i.v. injection with the ND nanozymes (dose: 10 mg/kg). (C) UV-vis-NIR absorption spectra of ND nanozymes in pure water over time. (D) The degradation rate of ND nanozymes in different physiological solutions (pure water, normal saline, PBS, PBS pH = 6.5, RPMI containing 10% serum) on the sixth day. (E) Photographs of ND nanozymes in physiological solutions at various time points. (F) TEM images of ND nanozymes in pure water on the 0 and fourth day. (G–I) XPS spectra of ND nanozymes in pure water on the fourth day; core level spectra of (G) Ni 2p, (H) S 2p, and (I) O 1s. (J) The degradation mechanism of ND nanozymes *in vivo*.
See also Figures S11 and S12.

collected for H&E staining (Figure 9C). No obvious inflammation and edema were observed in these main organs, indicating that there was no obvious tissue damage and the satisfactory histocompatibility. Considering the rapid *in vivo* degradation of ND nanozymes, it is possible to conclude that there is no long-term toxicity of the biodegradable ND nanozymes, which highlights their enormous potential for clinical bacterial application.

DISCUSSION

In summary, monodisperse ND nanozymes were prepared through a simple solvothermal method based on the La Mer scheme, which have satisfactory photothermal performance, high photothermal conversion efficiency, excellent peroxide-like catalytic activity, and GSH-depleting function. The as-obtained ND nanozymes as HRP-like nanozymes could generate •OH in the presence of H_2O_2 through Fenton-like reaction, and the catalytic activity of Fenton-like reaction was further enhanced by the mild photothermal performance generated by PTT, which led to the achievement of photothermall-enhanced catalytic bacterial treatment *in vitro*. More importantly, the experimental results of wound healing *in vivo* displayed that the synergetic antimicrobials could be used to disinfect wounds. Moreover, the ND nanozymes acted as GSH-like mimetic enzymes, thus possessing prominent GSH-depleting function, which could effectively consume some reducing substances in bacteria, resulting in better antibacterial effects. Interestingly, these novel ND nanozymes owing to their rapid degradation properties could be rapidly metabolized by the renal and fecal pathways, without causing any significant toxicity. Collectively, the ND nanozymes as biodegradable multifunctional antibacterial agents have a wide application prospect in precise sterilization.

Limitations of the Study

Although biodegradable ND nanozymes achieved significant synergistic antibacterial effect *in vitro* and *in vivo*, their synergistic mechanism of antibacterial treatment and the biodegradable mechanism still need to be further explored.

Resource Availability

Lead Contact

Further information and requests for resources and reagents should be directed to and will be fulfilled by the Lead Contact, Prof. Liang Cheng (lcheng2@suda.edu.cn).

Materials Availability

This study did not generate new unique reagents.

Data and Code Availability

This study did not generate datasets/code.

METHODS

All methods can be found in the accompanying Transparent Methods supplemental file.

SUPPLEMENTAL INFORMATION

Supplemental Information can be found online at https://doi.org/10.1016/j.isci.2020.101281.
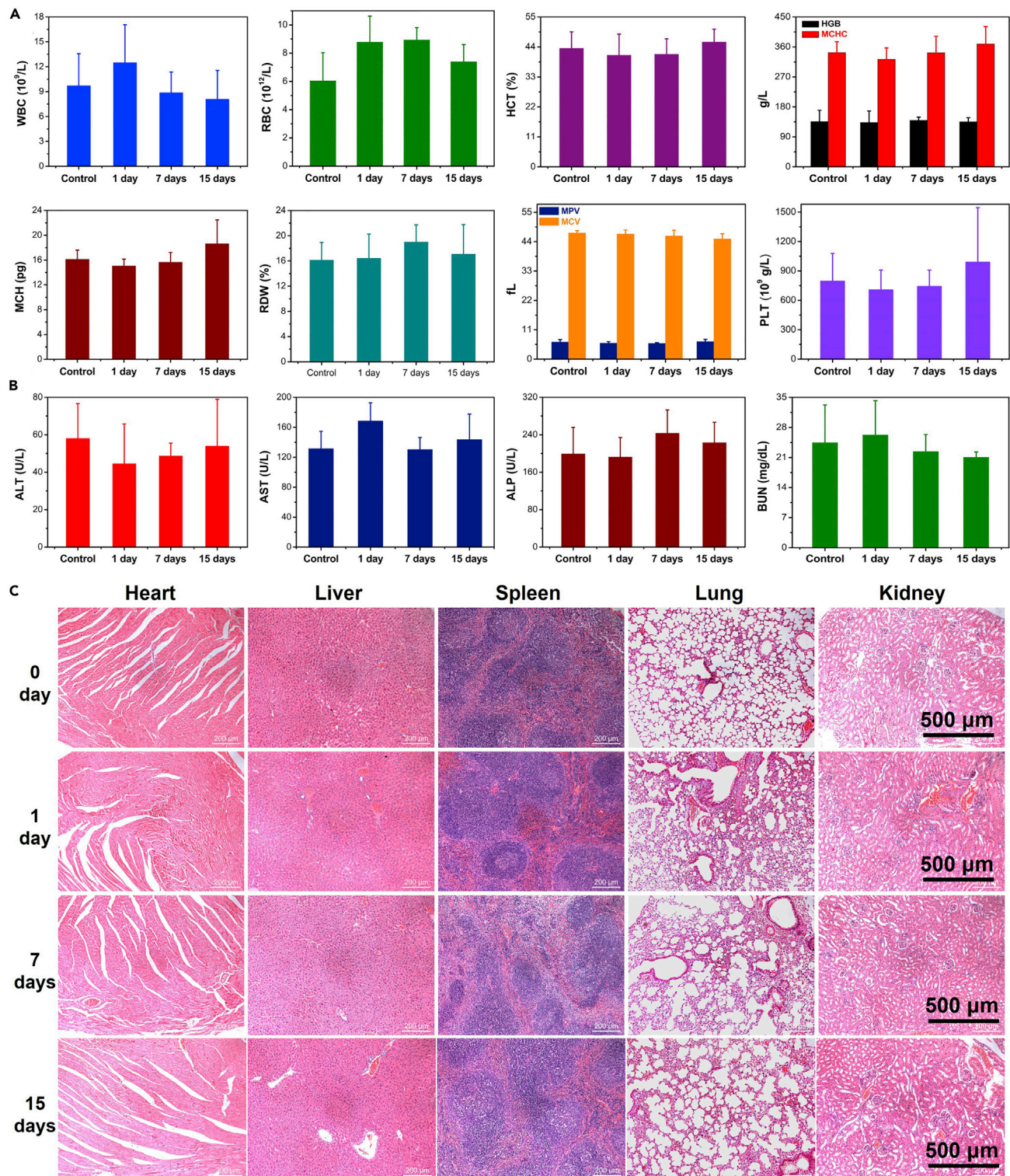
Figure 9. Biosafety Evaluation of the ND Nanozymes

(A–C) (A) The blood panel analysis and (B) the blood biochemistry test. (C) H&E staining images of major organs (including heart, liver, spleen, lung, and kidney) of the mice after i.v. injection of ND nanozymes at different days (dose: 10 mg/kg).

See also Figure S13.

AUTHOR CONTRIBUTIONS

Conceptualization, Xianwen Wang; Methodology, Xianwen Wang and L.F.; Investigation, Xianwen Wang, L.F., Y.S., Xiyu Wang., X.Z., Q.S., F.G., Y.Y., Y.M., and Z.M.; Writing – Original Draft, Xianwen Wang; Writing – Review & Editing, Xianwen Wang, L.C., and Z.Z.; Resources, L.C. and Z.Z.; Supervision, L.C. and Z.Z.

DECLARATION OF INTERESTS

The authors declare no competing interests.

REFERENCES

Cao, F., Zhang, L., Wang, H., You, Y., Wang, Y., Gao, N., Ren, J., and Qu, X. (2019). Defect-rich adhesive nanozymes as efficient antibiotics for enhanced bacterial inhibition. Angew. Chem. Int. Ed. 58, 16236–16242.

Chen, J., Shu, Y., Li, H., Xu, Q., and Hu, X. (2018). Nickel metal-organic framework 2D nanosheets with enhanced peroxidase nanozyme activity for colorimetric detection of H_2O_2. Talanta 189, 254–261.

De Zoysa, M., Pushpamali, W.A., Oh, C., Whang, I., Kim, S.J., and Lee, J. (2008). Transcriptional up-regulation of disk abalone selenium dependent glutathione peroxidase by H_2O_2 oxidative stress and vibrio alginolyticus bacterial infection. Fish Shellfish Immunol. 25, 446–457.

Gao, Q., Zhang, X., Yin, W., Ma, D., Xie, C., Zheng, L., Dong, X., Mei, L., Yu, J., Wang, C., et al. (2018). Functionalized MoS_2 nanovehicle with near-infrared laser-mediated nitric oxide release and photothermal activities for advanced bacteria-infected wound therapy. Small 14, 1802290.

He, C.-F., Wang, S.-H., Yu, Y.-J., Shen, H.-Y., Zhao, Y., Gao, H.-L., Wang, H., Li, L.-L., and Liu, H.-Y. (2016). Advances in biodegradable nanomaterials for photothermal therapy of cancer. Cancer Biol. Med. 13, 299.

He, G., Ma, Y., Zhou, H., Sun, S., Wang, X., Qian, H., Xu, Y., Miao, Z., and Zha, Z. (2019). Mesoporous NiS_2 nanospheres as a hydrophobic anticancer drug delivery vehicle for synergistic photothermal-chemotherapy. J. Mater. Chem. B 7, 143–149.

Huo, M., Wang, L., Zhang, H., Zhang, L., Chen, Y., and Shi, J. (2019). Construction of single-iron-atom nanocatalysts for highly efficient catalytic antibiotics. Small 15, 1901834.

Liu, Y., Bhattarai, P., Dai, Z., and Chen, X. (2019a). Photothermal therapy and photoacoustic imaging via nanotheranostics in fighting cancer. Chem. Soc. Rev. 48, 2053–2108.

Liu, Y., Guo, Z., Li, F., Xiao, Y., Zhang, Y., Bu, T., Jia, P., Zhe, T., and Wang, L. (2019b). Multifunctional magnetic copper ferrite nanoparticles as Fenton-like reaction and near-infrared photothermal agents for synergetic antibacterial therapy. ACS Appl. Mater. Interfaces 11, 31649–31660.

Liu, Y., Lin, A., Liu, J., Chen, X., Zhu, X., Gong, Y., Yuan, G., Chen, L., and Liu, J. (2019c). Enzyme-responsive mesoporous ruthenium for combined chemo-photothermal therapy of drug-resistant bacteria. ACS Appl. Mater. Interfaces 11, 26590–26606.

Liu, Y., Zhen, W., Wang, Y., Liu, J., Jin, L., Zhang, T., Zhang, S., Zhao, Y., Yin, N., Niu, R., et al. (2019d). Double switch biodegradable porous hollow trinickel monophosphide nanospheres for multimodal imaging guided photothermal therapy. Nano Lett. 19, 5093–5101.

Liu, G., Zhang, Q., Li, Y., Wang, X., Wu, H., Wei, Y., Zeng, Y., and Tao, L. (2020). High-throughput preparation of antibacterial polymers from natural product derivatives via the hantzsch reaction. iScience 23, 100754.

Miao, Z., Fan, L., Xie, X., Ma, Y., Xue, J., He, T., and Zha, Z. (2019). Liquid exfoliation of atomically thin antimony selenide as an efficient two-dimensional antibacterial nanoagent. ACS Appl. Mater. Interfaces 11, 26664–26673.

Qing, G., Zhao, X., Gong, N., Chen, J., Li, X., Gan, Y., Wang, Y., Zhang, Z., Zhang, Y., Guo, W., et al. (2019). Thermo-responsive triple-function nanotransporter for efficient chemo-photothermal therapy of multidrug-resistant bacterial infection. Nat. Commun. 10, 1–12.

Sang, Y., Li, W., Liu, H., Zhang, L., Wang, H., Liu, Z., Ren, J., and Qu, X. (2019). Construction of nanozyme-hydrogel for enhanced capture and elimination of bacteria. Adv. Funct. Mater. 29, 1900518.

Shan, J., Li, X., Yang, K., Xiu, W., Wen, Q., Zhang, Y., Yuwen, L., Weng, L., Teng, Z., and Wang, L. (2019). Efficient bacteria killing by Cu_2WS_4 nanocrystals with enzyme-like properties and bacteria-binding ability. ACS Nano 13, 13797–13808.

Tang, Z., Zhang, H., Liu, Y., Ni, D., Zhang, H., Zhang, J., Yao, Z., He, M., Shi, J., and Bu, W. (2017). Antiferromagnetic pyrite as the tumor microenvironment-mediated nanoplatform for self-enhanced tumor imaging and therapy. Adv. Mater. 29, 1701683.

Wang, X., Li, F., Yan, X., Ma, Y., Miao, Z.-H., Doug, L., Chen, H., Lu, Y., and Zha, Z. (2017). Ambient aqueous synthesis of ultrasmall $Ni_{0.85}Se$ nanoparticles for noninvasive photoacoustic imaging and combined photothermal-chemotherapy of cancer. ACS Appl. Mater. Interfaces 9, 41782–41793.

Wang, L., Zhang, X., Yu, X., Gao, F., Shen, Z., Zhang, X., Ge, S., Liu, J., Gu, Z., and Chen, C. (2019a). An all-organic semiconductor C_3N_4/PDINH heterostructure with advanced antibacterial photocatalytic therapy activity. Adv. Mater. 31, 1901965.

Wang, X., Zhong, X., Lei, H., Geng, Y., Zhao, Q., Gong, F., Yang, Z., Dong, Z., Liu, Z., and Cheng, L. (2019b). Hollow Cu_2Se nanozymes for tumor photothermal-catalytic therapy. Chem. Mater. 31, 6174–6186.

Wang, X., Zhong, X., Bai, L., Xu, J., Gong, F., Dong, Z., Yang, Z., Zeng, Z., Liu, Z., and Cheng, L. (2020a). Ultrafine titanium monoxide (TiO_{1+x}) nanorods for enhanced sonodynamic therapy. J. Am. Chem. Soc. 142, 6527–6537.

Wang, X., Zhong, X., Zha, Z., He, G., Miao, Z., Lei, H., Luo, Q., Zhang, R., Liu, Z., and Cheng, L. (2020b). Biodegradable CoS_2 nanoclusters for photothermal-enhanced chemodynamic therapy. Appl. Mater. Today 18, 100464.

Wentao, W., Tao, Z., Bulei, S., Tongchang, Z., Qicheng, Z., Fan, W., Ninglin, Z., Jian, S., Ming, Z., and Yi, S. (2019). Functionalization of polyvinyl alcohol composite film wrapped in Am-ZnO@CuO@Au nanoparticles for antibacterial application and wound healing. Appl. Mater. Today 17, 36–44.

Wu, S., Li, A., Zhao, X., Zhang, C., Yu, B., Zhao, N., and Xu, F.-J. (2019). Silica-coated gold-silver nanocages as photothermal antibacterial agents for combined anti-infective therapy. ACS Appl. Mater. Interfaces 11, 17177–17183.

Xi, J., Wei, G., An, L., Xu, Z., Xu, Z., Fan, L., and Gao, L. (2019a). Copper/carbon hybrid nanozyme: tuning catalytic activity by the copper state for antibacterial therapy. Nano Lett. 19, 7645–7654.

Xi, J., Wei, G., Wu, Q., Xu, Z., Liu, Y., Han, J., Fan, L., and Gao, L. (2019b). Light-enhanced sponge-like carbon nanozyme used for synergetic antibacterial therapy. Biomater. Sci. 7, 4131–4141.

Xu, Z., Qiu, Z., Liu, Q., Huang, Y., Li, D., Shen, X., Fan, K., Xi, J., Gu, Y., Tang, Y., et al. (2018).

Converting organosulfur compounds to inorganic polysulfides against resistant bacterial infections. Nat. Commun. 9, 3713.

Xu, B., Wang, H., Wang, W., Gao, L., Li, S., Pan, X., Wang, H., Yang, H., Meng, X., Wu, Q., et al. (2019). A single-atom nanozyme for wound disinfection applications. Angew. Chem. Int. Ed. 58, 4911–4916.

Yan, J., Ralston, M.M., Meng, X.M., Bongiovanni, K.D., Jones, A.L., Benndorf, R., Nelin, L.D., Frazier, W.J., Rogers, L.K., Smith, C.V., et al. (2013). Glutathione reductase is essential for host defense against bacterial infection. Free Radic. Biol. Med. 61, 320–332.

Yan, L., Zhao, F., Wang, J., Zu, Y., Gu, Z., and Zhao, Y. (2019). A safe-by-design strategy towards safer nanomaterials in nanomedicines. Adv. Mater. 31, 1805391.

Yang, B., Chen, Y., and Shi, J. (2019a). Nanocatalytic medicine. Adv. Mater. 31, 1901778.

Yang, G., Phua, S.Z.F., Bindra, A.K., and Zhao, Y. (2019b). Degradability and clearance of inorganic nanoparticles for biomedical applications. Adv. Mater. 31, 1805730.

Yang, Y., Deng, Y., Huang, J., Fan, X., Cheng, C., Nie, C., Ma, L., Zhao, W., and Zhao, C. (2019c). Size-transformable metal–organic framework–derived nanocarbons for localized chemo-photothermal bacterial ablation and wound disinfection. Adv. Funct. Mater. 29, 1900143.

Yin, W., Yu, J., Lv, F., Yan, L., Zheng, L.R., Gu, Z., and Zhao, Y. (2016). Functionalized nano-MoS$_2$ with peroxidase catalytic and near-infrared photothermal activities for safe and synergetic wound antibacterial applications. ACS Nano 10, 11000–11011.

Yong, Y., Zhou, L., Gu, Z., Yan, L., Tian, G., Zheng, X., Liu, X., Zhang, X., Shi, J., and Cong, W. (2014). WS$_2$ nanosheet as a new photosensitizer carrier for combined photodynamic and photothermal therapy of cancer cells. Nanoscale 6, 10394–10403.

Zhang, S., Sun, C., Zeng, J., Sun, Q., Wang, G., Wang, Y., Wu, Y., Dou, S., Gao, M., and Li, Z. (2016). Ambient aqueous synthesis of ultrasmall PEGylated Cu$_{2-x}$Se nanoparticles as a multifunctional theranostic agent for multimodal imaging guided photothermal therapy of cancer. Adv. Mater. 28, 8927–8936.

Zhang, W., Yang, C., Lei, Z., Guan, G., He, S.-A., Zhang, Z., Zou, R., Shen, H., and Hu, J. (2019a). New strategy for specific eradication of implant-related infections based on special and selective degradability of rhenium trioxide nanocubes. ACS Appl. Mater. Interfaces 11, 25691–25701.

Zhang, Y., Liu, W., Li, Y., Yang, Y.-W., Dong, A., and Li, Y. (2019b). 2D graphdiyne oxide serves as a superior new generation of antibacterial agents. iScience 19, 662–675.

Zhong, X., Wang, X., Cheng, L., Zhan, G., Gong, F., Zhang, R., Hu, J., Liu, Z., and Yang, X. (2020). GSH-depleted PtCu$_3$ nanocages for chemodynamic-enhanced sonodynamic cancer therapy. Adv. Funct. Mater. 30, 1907954.

Supplemental Information

Biodegradable Nickel Disulfide Nanozymes

with GSH-Depleting Function for High-Efficiency

Photothermal-Catalytic Antibacterial Therapy

Xianwen Wang, Linxin Fan, Liang Cheng, Yanbin Sun, Xiyu Wang, Xiaoyan Zhong, Qianqian Shi, Fei Gong, Yu Yang, Yan Ma, Zhaohua Miao, and Zhengbao Zha

Supplementary information

Biodegradable nickel disulfide nanozymes with GSH-depleted function for high-efficiency photothermal-catalytic antibacterial therapy

Xianwen Wang[1,2], Linxin Fan[1], Liang Cheng[2,4]*, Yanbin Sun[1], Xiyu Wang[2], Xiaoyan Zhong[3], Qianqian Shi[1], Fei Gong[2], Yu Yang[2], Yan Ma[1], Zhaohua Miao[1], and Zhengbao Zha[1]*

[1]School of Food and Biological Engineering, Hefei University of Technology, Hefei, 230009, P. R. China.

[2]Institute of Functional Nano & Soft Materials (FUNSOM), Jiangsu Key Laboratory for Carbon-based Functional Materials and Devices, Soochow University, Suzhou 215123, P. R. China

[3]National Engineering Research Centre for Nanomedicine, College of Life Science and Technology, Huazhong University of Science and Technology, Wuhan 430074, P. R. China.

[4]Lead Contact

Corresponding Author:

*E-mail: zbzha@hfut.edu.cn (Z. Zha), Phone: +86-551-62901285

*E-mail: lcheng2@suda.edu.cn (L. Cheng), Phone: +86-512-65880927 (Lead Contact)

Transparent Methods

Materials and reagents: Polyvinylpyrrolidone (PVP, K30, MW=40000), hydrogen peroxide (H_2O_2, 30 wt%), and sodium thiosulfate pentahydrate ($Na_2S_2O_3\cdot5H_2O$) were obtained from Sinopharm Chemical Reagent Co., Ltd. Nickel nitrate hexahydrate ($Ni(NO_3)_2\cdot6H_2O$) was purchased from Aladdin Chemical Reagent Co., Ltd. 3-(4,5-dimethyl-2-thiazolyl)-2,5-diphenyl-2-Htetrazolium bromide (MTT), O-phenylenediamine (OPDA), 5, 5'-dithio-bis (2-nitrobenzoic acid) (DTNB), and 3, 3', 5, 5'-Tetramethylbenzidine (TMB) were bought from J&K Chemical Co., Ltd. All reagents were purchased from commercial sources and used without any further purification.

Bacteria: Escherichia coli (E. coli, DH5α) and methicillin-resistant staphylococcus aureus (MRSA, Mu50). The reason for choosing these two bacteria for the following reason: E. coli and MRSA are representative of Gram positive and negative bacteria, and the separation rate of these two bacteria is the best among the positive and negative bacteria, respectively. These two kinds of bacteria are easy to be separated and their purity are high. E. coli (DH5α) is a mutagenic strain, which mainly shows a lack of immunity to exogenous DNA, and it doesn't emerge drug resistance. Therefore, it can be used as a typical representative for studying non-resistant bacteria. MRSA, as a relatively common drug-resistant bacteria, has a high pathogenic rate and multiple transmission routes, which can cause many diseases and pose a certain threat to people's health and safety. The mu50 strain was discovered earlier and was one of the first three bacteria to have DNA sequence completely. It is safe and controllable for use in studies, and it is not particularly pathogenic. Based on this, it is reasonable to choose these two bacteria based on these considerations.

Synthesis of ND nanozymes: ND nanozymes were prepared by a simple solvothermal method based on our previously reported strategy. (He et al., 2019) Briefly, 0.3 g PVP, 1.0 mmol $Ni(NO_3)_2\cdot6H_2O$ (0.291 g), and 3.0 mmol $Na_2S_2O_3\cdot5H_2O$ (0.745 g) were completely dissolved in a mixture of 20 mL of ultrapure water and 20 mL of ethylene glycol under vigorous magnetic stirring. Thereafter, the mixed solution was put into the Teflon-lined sealed autoclave and stewed at 180 °C for 12 h. The products were obtained through thorough centrifugation/washing cycles. Next, the as-obtained ND nanozymes were further dialyzed for 24 h to remove the unreacted materials, and the final products were stored at -4 °C protected by N_2 for further use.

Characterizations of ND nanozymes: Transmission electron microscope (TEM, JEM-2100F, Japan), energy-dispersive X-ray spectroscopy (EDS) (Tecnal G2 F20 U-Twin), and high-angle annular dark-field scanning TEM (HAAD-FSTEM) were obtained to characterize morphology, structure, and composition of ND nanozymes. The crystalline structure of ND nanozymes was performed by X-ray diffraction (XRD, Panalytical Empyrean). The surface chemistry composition and chemical states of ND nanozymes were determined by X-ray photoelectron spectroscopy (XPS, ESCALab 250Xi). UV–vis–NIR spectrophotometer (Genesys™ 10S UV–vis, Thermo Scientific) was used to measure UV-vis-NIR absorption spectra of samples. The photothermal data and thermal imaging pictures were recorded by using an IR thermal camera (Fortric 225).

Photothermal performance of ND nanozymes: To evaluate the photothermal effect of ND nanozymes, 1.0 mL aqueous solution of ND nanozymes with different concentrations (0-75 μg/mL) were added in quartz cells and irradiated by 808 nm laser with different power densities (0.2-1.5 W/cm^2) for 10 min, respectively. The photothermal stability of ND nanozymes was determined by six laser on/off cycles irradiation, and the photothermal conversion efficiency of ND nanozymes was calculated using the methods previously described.(Wang et al., 2019b)

Peroxides-like catalytic activity of ND nanozymes: The •OH was analyzed according to the principle that •OH could oxide TMB or OPDA probe and strengthen the absorbance of TMB at 664 nm or OPDA at 414 nm.(Wang et al., 2020) Briefly, the TMB and OPDA were used as the indicators to visualize and monitor the •OH generation. In detail, 1.0 mL acetate buffer containing ND nanozymes (20 μg/mL), TMB (0.5 mM), and H_2O_2 with different concentrations (0-1.0 mM) was incubated for 30 min at room temperature (25 °C). The color of the solution was imaged and the UV-vis-NIR spectra was measured. The catalytic performance of ND nanozymes at 45 °C was further explored to simulate the effect of catalytic property by the mild photothermal treatment.

Calculation of the Michaelis–Menten constant (K$_M$) and maximum velocity (V$_{max}$): Results based on TMB tests were used to calculate K$_M$ and V$_{max}$, all average initial velocities of absorbance changes would then be converted as initial velocities (v$_0$) of cation-free radical production or hydroxyl radical formation via the Beer Lambert law **(Eq. 1)**, which were then plotted against the corresponding

concentration and fitted with Michaelis Menten curves **(Figure S8a) (Eq. 2)**. Moreover, to determine

the K_M and V_{max}, a linear double-reciprocal plot **(Lineweaver Burk plot, Eq. 3)** was obtained as given

in **Figure S8b**. According to the calculation, the K_M and V_{max} values were calculated to be 3.64 mM

and 1.55×10^{-4} mM min^{-1} for ND nanozymes.

$$A = kbc \quad \textbf{(Eq. 1)}$$

$$v_0 = \frac{V_{max} \bullet [S]}{K_m + [S]} \quad \textbf{(Eq. 2)}$$

$$\frac{1}{v_0} = \frac{K_m}{V_{max}} \bullet \frac{1}{[S]} + \frac{1}{V_{max}} \quad \textbf{(Eq. 3)}$$

GSH-depleted property of ND nanozymes: The consumption of GSH was detected with DTNB

probe by UV–vis–NIR spectroscopy.(Wan et al., 2019) The as-obtained ND nanozymes with different

concentrations (0.1 mM or 1.0 mM) were mixed with GSH (1.0 mM) at room temperature. At different

points, 100 μL of the mixture was added into 900 μL phosphate buffer saline (PBS, pH 7.4), and then

DTNB (0.1 mM) was added the mixed solution. After 2 min later, the absorbance spectrum of this

mixed solution was recorded by UV–vis–NIR spectrophotometer.

In vitro **cytotoxicity experiments:** Human umbilical vein endothelial cells (HUVECs) were used for

evaluation the cytotoxicity of ND nanozymes. Briefly, the HUEVCs with the density of 1×10^4 cells

for each well were seeded into 96-well plates for 24 h. Then the cells incubated with ND nanozymes

with the varying concentrations (0-100 μg/mL) and cultured for another 12 h. Finally, the relative cell

viabilities were determined using a standard MTT method. (Guan et al., 2019; Wang et al., 2019b)

In vitro **antibacterial experiments:** During antibacterial investigations, Escherichia coli (*E. coli*,

DH5α) was used as the model Gram (-) bacterial and methicillin-resistant staphylococcus aureus

(MRSA, Mu50) as model Gram (+) bacterial cell strains. The strains were revived from frozen glycerol

stocks by inoculation in Luria−Bertani (LB) medium overnight at 37 ºC in a humidified incubator. The

population density of the bacterial cells was determined by measuring the absorbance at 600 nm. In a

typical antibacterial assay, *E. coli* or MRSA were divided into following eight groups: (1) bacteria; (2)

bacteria + NIR light; (3) bacteria + H_2O_2; (4) bacteria + NIR light + H_2O_2; (5) bacteria + ND

nanozymes; (6) bacteria + ND nanozymes + H_2O_2; (7) bacteria + ND nanozymes + NIR light; (8)

bacteria + ND nanozymes + H₂O₂ + NIR light. The groups of (2), (4), (7)-(8) were further exposed to NIR laser (808 nm, 1.0 W/cm^2) for 3 min. After the NIR irradiation, the procedure was the same as groups of (1), (3), (5)-(6). The final concentrations of ND nanozymes, H₂O₂, and bacteria were 100 μg/mL, 200 μM, and 1×10^6 colony forming units (CFU)/mL, respectively. The total volume of solution in each well was 0.5 mL. After incubation for 20 min, 100 μL of bacterial suspension of groups (1)-(8) were spread on the agar culture plate and incubated at 37 ^{o}C for 18 h, and the number of colonies was counted. All experiments were repeated for three times. The bacteria survival rate was calculated using the following equation: Survival viability (%) = $N_t/N_c \times 100\,\%$, where N_t represents the number of colonies formed in the experimental group and N_c refers to the number of colonies formed in the control group (PBS group). (Liu et al., 2019)

Live/dead staining test: The bacteria after various treatments stained with SYTO9 and propidium iodide (PI) for 30 min, followed by washing three times using PBS. Fluorescence microscopy was used to observe the live (green fluorescence) and dead (red fluorescence) bacterial by the fluorescence microscopy. (Miao et al., 2019)

ROS staining test: The method to study ROS generation in bacterial was tested using a modified 2', 7'-dichlorodihydrofluorescein diacetate (DCFH-DA) probe. The bacteria after different treatments stained with DCFH-DA (20 μM) for 30 min, followed by washing three times using PBS. After that, green fluorescence was observed using fluorescence microscope to prove the generation of ROS.

Morphological observation of the bacteria: Bacterial samples were centrifuged (4000 rpm, 3 min) and re-dispersed into 2.5% glutaraldehyde after respective treatments. After 12 h, the fixed samples were further dehydrated gradually using ethanol solution with increasing ethanol concentration (10%, 30%, 50%, 70%, and 90%) for 10 min each. Finally, the cell samples were dispersed in 200 μL ethanol and dipped on a carbon coated cooper grid for scanning electron microscope (SEM, FEI Quanta 200F) observation.

***In vivo* antibacterial activity and wound healing:** All the animal procedures were performed in compliance with the guidelines of the Institutional Animal Care and Use Committee of Department of Anhui Medical University (LLSC20150134). Mice were divided into following six groups randomly (n = 5): (1) control; (2) H₂O₂; (3) ND nanozymes; (4) ND nanozymes + H₂O₂; (5) ND nanozymes +

5

NIR light; (6) ND nanozymes + H_2O_2 + NIR light. These mice their right flanks shaved, followed by anesthetization with pentobarbital sodium. A skin wound ~ 100 mm^2 was created by nicking with sterile scalpel. Then, the MRSA suspension (50 μL, 1×10^9 CFU/mL) was gradually inoculated onto the wound and the moisture allowed to evaporate naturally. After 12 h, for the ND nanozymes + H_2O_2 + NIR light treatment group, 50 μL of ND nanozymes (100 μg/ml, dispersed into PBS) and 50 μL of H_2O_2 (200 μM, dispersed into PBS) were dropped onto the bacterial foci, then the wound was irradiated with an NIR laser (808 nm, 1.0 W/cm^2) for 3 min. Similarly, the other five groups were administered using the same procedure. After different treatments, the body weight of mice was recorded and the wound sizes of mice in all groups were measured perpendicularly ($d_1 \leq d_2$) using the digital caliper. The wound area (S) was calculated according to the following equation: $S = \pi d_1 d_2 / 4$. (Huo et al., 2019) At 5 days, the skin samples on mice were dissected for histopathological H&E staining and Masson's trichrome staining analysis. Additionally, any mouse of each group was dissected and the main organs (heart, liver, spleen, lung, and kidney) were collected for hematoxylin and eosin (H&E) staining analysis of biocompatibility. (Wang et al., 2018)

***In vivo* toxicity, biodistribution, and metabolism:** The *in vivo* toxicity of ND nanozymes was preliminarily evaluated by serum biochemistry and a complete blood panel test. In brief, ND nanozymes (10 mg/kg, 100 μL) were intravenously injected into three groups (five mice per group) of healthy Balb/c mice. At the 1st, 7th, and 15th day after injection, all five mice in each group were sacrificed to collect blood samples (~1.0 mL) for serum biochemistry and complete blood panel test. Another five healthy Balb/c mice treated only with PBS were used as control. The major organs (heart, liver, spleen, lung, and kidney) of those mice were dissected and divided into two halves for histological examination and biodistribution measurement, respectively. For histological examination, any mouse of each group was dissected and the main organs were collected for hematoxylin and eosin (H&E) staining. For biodistribution measurement, the major organs from the mice were solubilized by aqua regia for inductively coupled plasma-optical emission spectroscopy (ICP-OES) measurement to determine the Ni levels in these different organs. Additionally, to study the metabolic pathway, BALB/c mice intravenously injected with the ND nanozymes (10 mg/kg, 100 μL) were placed in the metabolism cages to collect their urine and fences at different time points, then solubilized by aqua regia for ICP-OES measurement to determine the Ni contents.
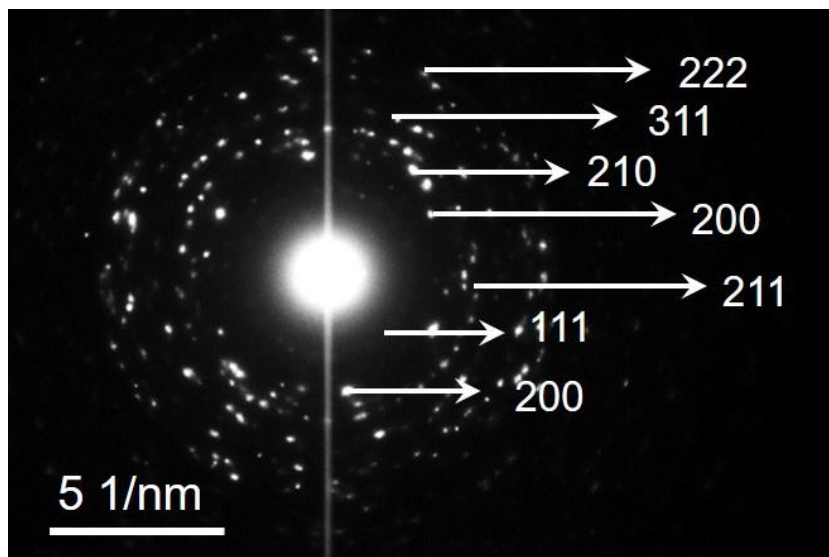
Supporting Figures

Figure S1. SAED image of the ND nanozymes. Related to Figure 1.
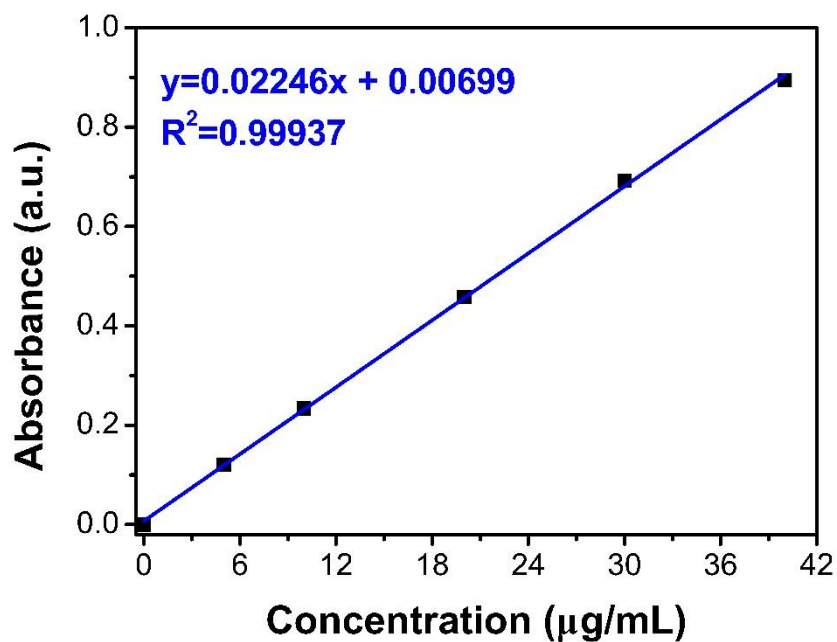

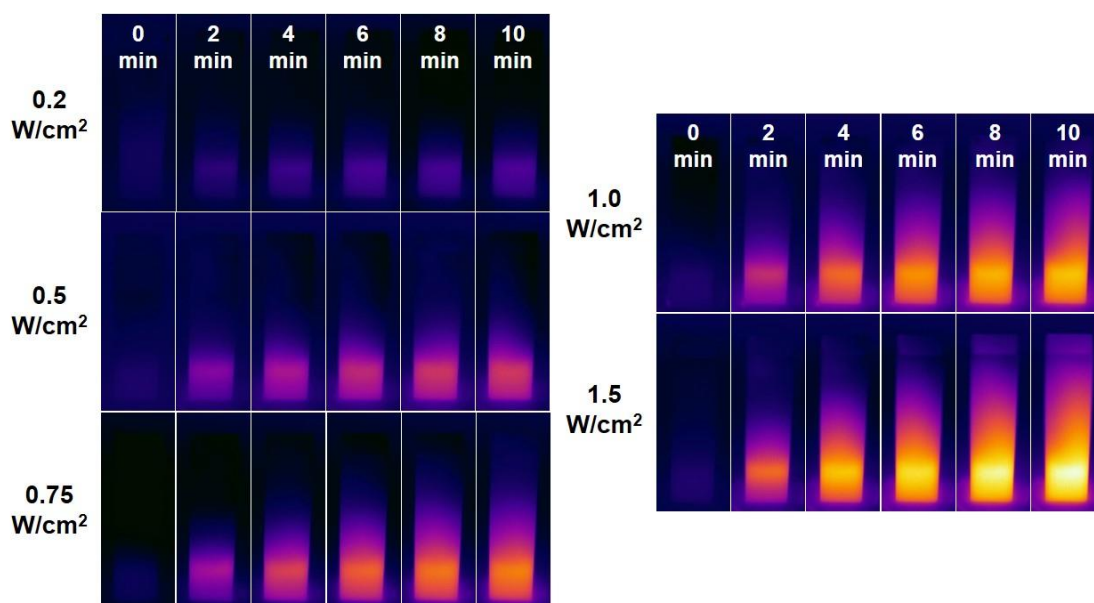**Figure S2.** The mass extinction coefficient of the ND nanozymes. Related to Figure 2.

Figure S3. Thermal images of ND nanozymes solution under 808 nm laser irradiation at different power densities (0.2, 0.5, 0.75, 1.0, and 1.5 W/cm^2) for 10 min. Related to Figure 2.
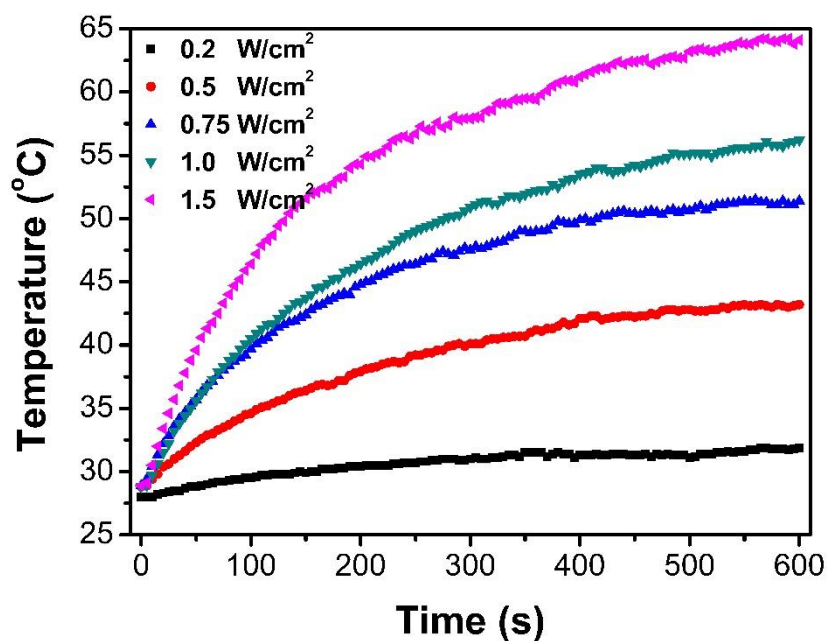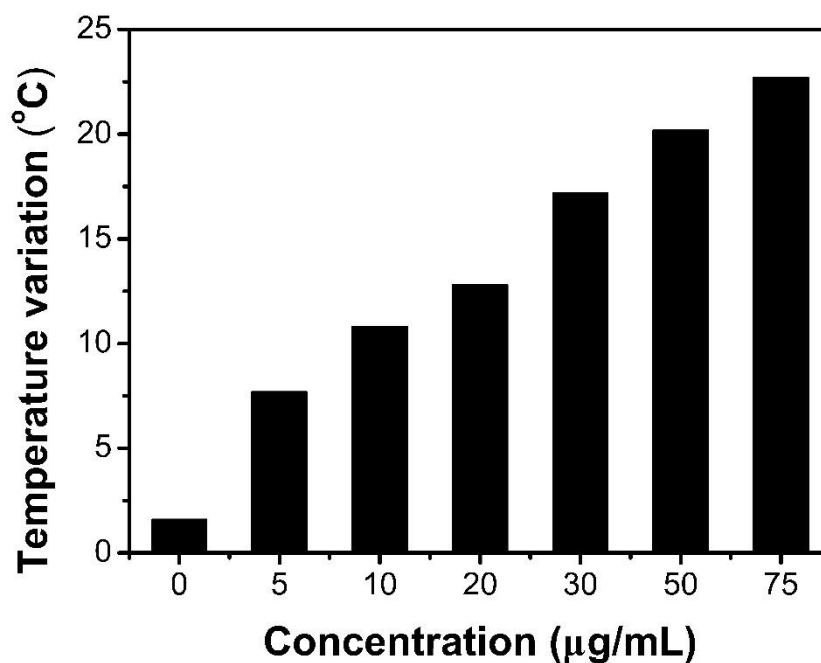

Figure S4. Temperature change curves of the ND nanozymes solution under 808 nm laser irradiation at different power densities (0.2, 0.5, 0.75, 1.0, and 1.5 W/cm^2) for 10 min. Related to Figure 2.

Figure S5. The plot of temperature variation over 10 min with different concentration of the ND nanozymes. Related to Figure 2.
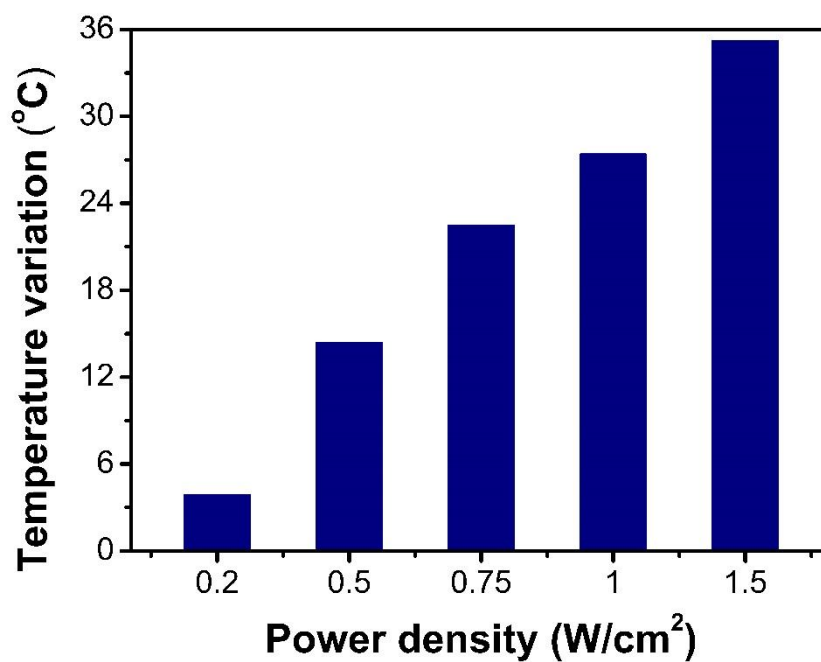
Figure S6. The plot of temperature variation over 10 min of ND nanozymes and with different power densities of 808 nm laser. Related to Figure 2.
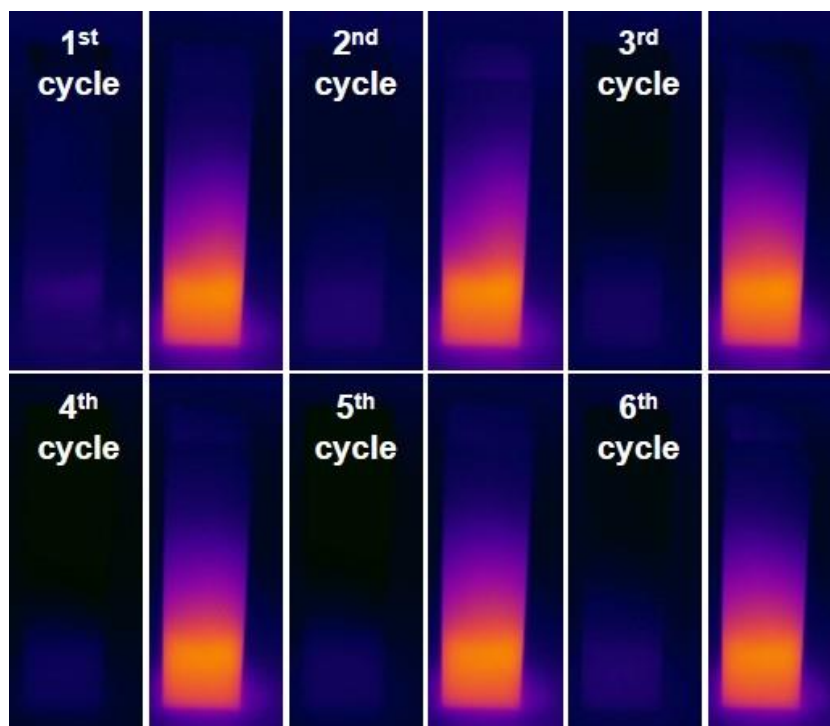
Figure S7. Starting temperature and maximum temperature of six cycles of laser irradiation. Related to Figure 2.
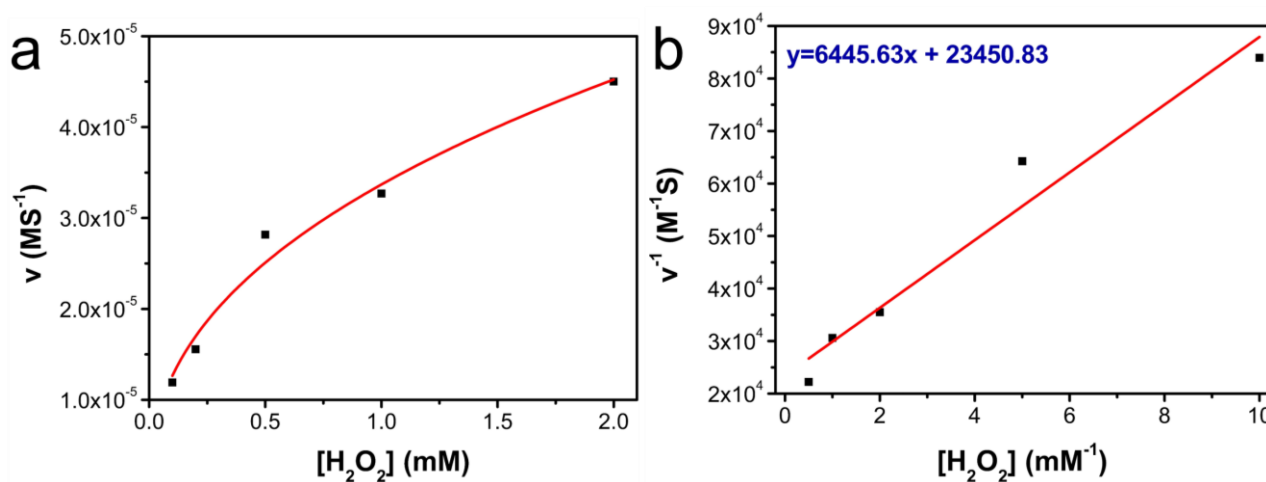

Figure S8. (a)The Michaelis-Menten fitting curves of initial hydroxyl radical generation velocities versus H_2O_2 concentration; (b) the Lineweaver-Burke fitting (double reciprocal) of Michaelis-Menten fitting curve. Related to Figure 3.
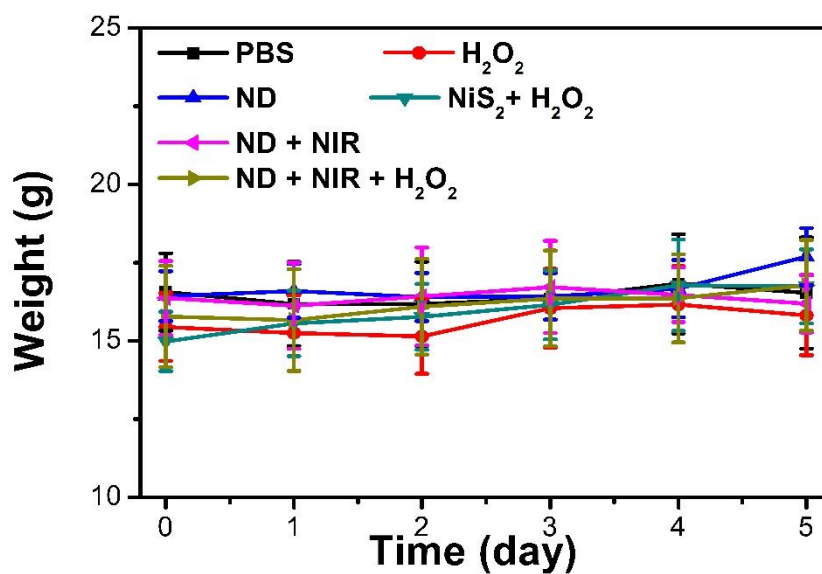
Figure S9. The body weights change during various treatments. Related to Figure 7.
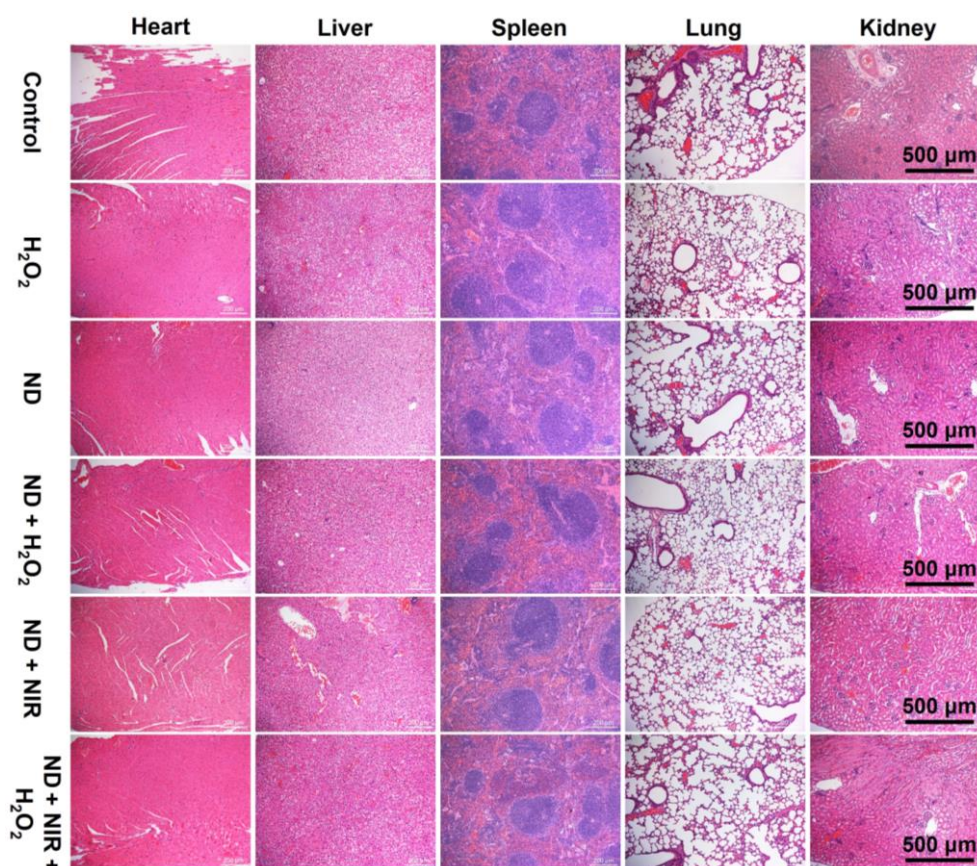

Figure S10. Toxicity evaluation of the ND nanozymes after antibacterial treatment *in vivo.* The H&E staining of the major organs (heart, liver, spleen, lung, and kidney) from mice after different treatments. Related to Figure 7.
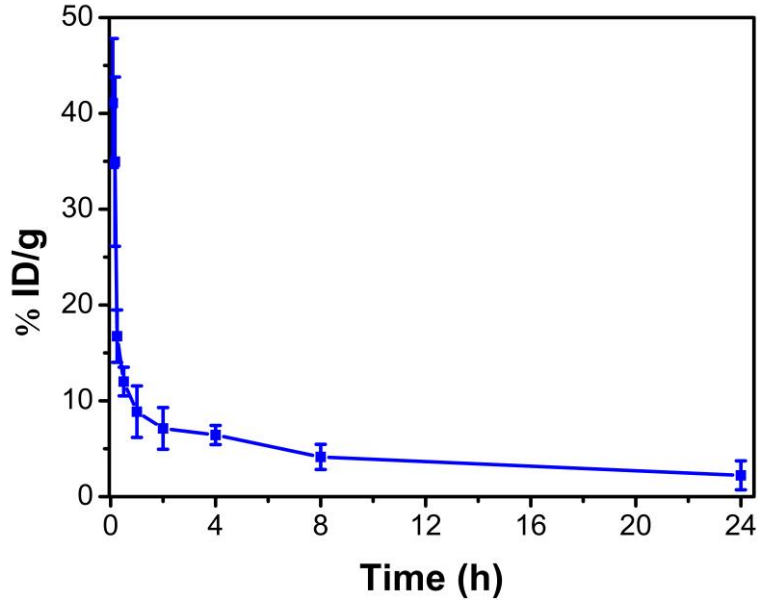
Figure S11. Blood circulation of ND nanozymes post i.v. injection. Related to Figure 8.
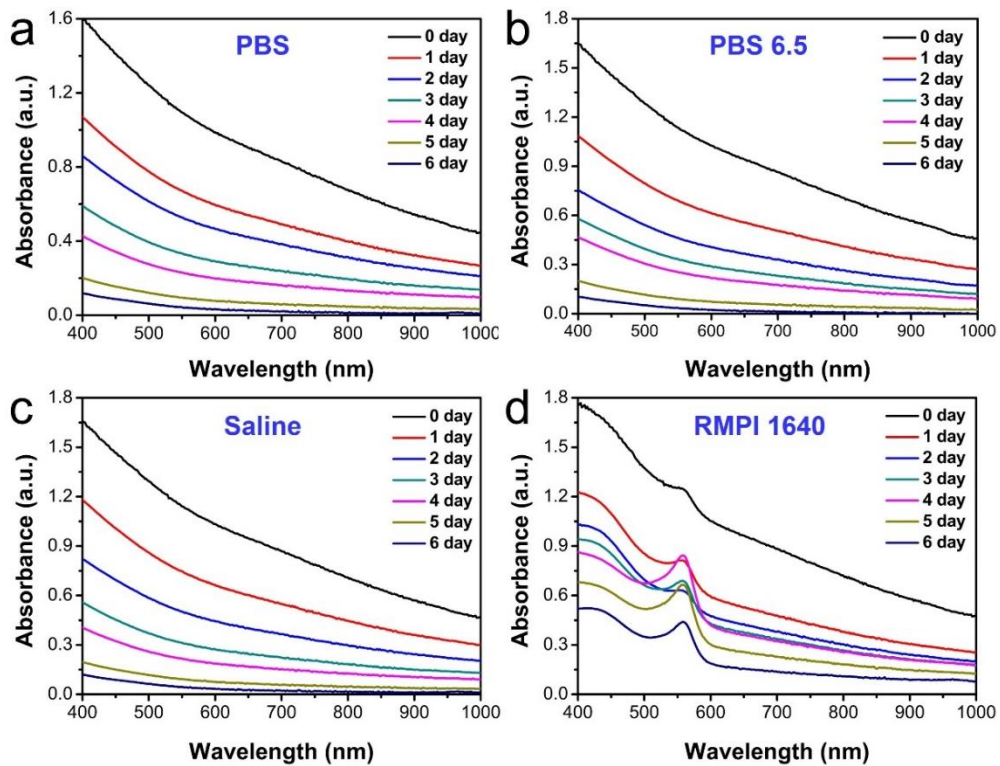

Figure S12. UV-vis-NIR absorption spectra of the ND nanozymes in (a) PBS, (b) PBS 6.5, (c) normal saline, (d) RMPI 1640 over time. Related to Figure 8.
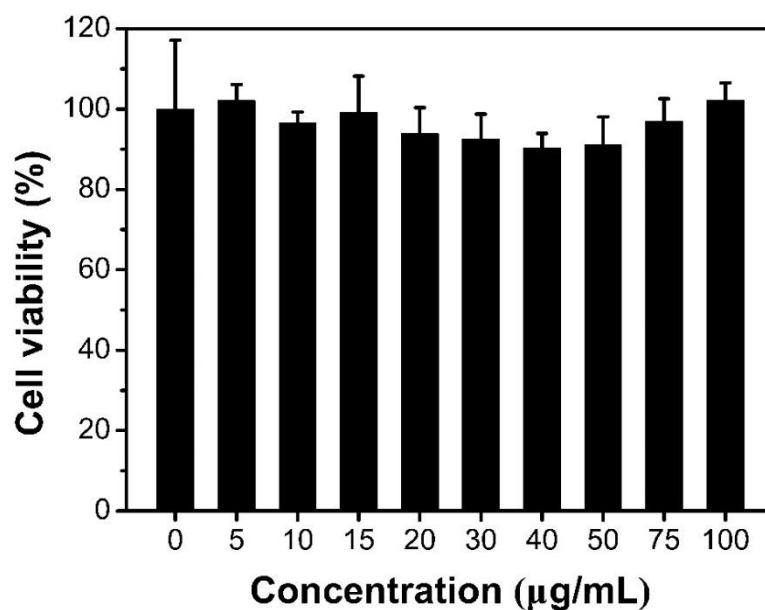
Figure S13. The relative cell viability of HUEVC after incubation with ND nanozymes. Related to Figure 9.

Table S1 Comparison of photothermal conversion efficiency. Related to Figure 2.

Materials	Photothermal conversion efficiency	Ref
Cu_2Te	33.1%	(Wang et al., 2017)
Cu_9S_5	25.7%	(Tian et al., 2011)
Prussian blue	32.2%	(Feng et al., 2019)
WS_2	32.83%	(Yong et al., 2014)
Graphene	25.9%	(Neelgund and Oki, 2016)
Black phosphorus	28.4%	(Sun et al., 2015)
$Au@TiO_2$	42.05%	(Gao et al., 2019)
Ti_3C_2	28.3%	(Tang et al., 2019)
V_2C	45.5%	(Cao et al., 2019)
Pt	52.5%	(Wang et al., 2019a)
Hollow MoS_2	34.46%	(Tan et al., 2016)
ND nanozymes	**43.8 %**	**This work**

References：

Cao, Y., Wu, T., Zhang, K., Meng, X., Dai, W., Wang, D., Dong, H., and Zhang, X. (2019). Engineered Exosome-Mediated Near-Infrared-II Region V_2C Quantum Dot Delivery for Nucleus-Target Low-Temperature Photothermal Therapy. ACS Nano *13*, 1499-1510.

Feng, T., Wan, J., Li, P., Ran, H., Chen, H., Wang, Z., and Zhang, L. (2019). A novel NIR-controlled NO release of sodium nitroprusside-doped Prussian blue nanoparticle for synergistic tumor treatment. Biomaterials *214*, 119213.

Gao, F., He, G., Yin, H., Chen, J., Liu, Y., Lan, C., Zhang, S., and Yang, B. (2019). Titania-coated 2D gold nanoplates as nanoagents for synergistic photothermal/sonodynamic therapy in the second near-infrared window. Nanoscale *11*, 2374-2384.

Guan, Q., Fu, D., Li, Y., Kong, X., Wei, Z., Li, W., Zhang, S., and Dong, Y. (2019). BODIPY-decorated nanoscale covalent organic frameworks for photodynamic therapy. iScience *14*, 180-198.

He, G., Ma, Y., Zhou, H., Sun, S., Wang, X., Qian, H., Xu, Y., Miao, Z., and Zha, Z. (2019). Mesoporous NiS_2 nanospheres as a hydrophobic anticancer drug delivery vehicle for synergistic photothermal-chemotherapy. J. Mater. Chem. B *7*, 143-149.

Huo, M., Wang, L., Zhang, H., Zhang, L., Chen, Y., and Shi, J. (2019). Construction of single-iron-atom nanocatalysts for highly efficient catalytic antibiotics. Small *15*, 1901834.

Liu, Y., Guo, Z., Li, F., Xiao, Y., Zhang, Y., Bu, T., Jia, P., Zhe, T., and Wang, L. (2019). Multifunctional magnetic copper ferrite nanoparticles as Fenton-like reaction and near-infrared photothermal agents for synergetic antibacterial therapy. ACS Appl. Mater. Interfaces *11*, 31649-31660.

Miao, Z., Fan, L., Xie, X., Ma, Y., Xue, J., He, T., and Zha, Z. (2019). Liquid exfoliation of atomically thin antimony selenide as an efficient two-dimensional antibacterial nanoagent. ACS Appl. Mater. Interfaces *11*, 26664-26673.

Neelgund, G.M., and Oki, A.R. (2016). Influence of carbon nanotubes and graphene nanosheets on photothermal effect of hydroxyapatite. J. Colloid Interface Sci. *484*, 135-145.

Sun, Z., Xie, H., Tang, S., Yu, X.-F., Guo, Z., Shao, J., Zhang, H., Huang, H., Wang, H., and Chu, P.K. (2015). Ultrasmall Black Phosphorus Quantum Dots: Synthesis and Use as Photothermal Agents. Angew. Chem. Inter. Ed. *54*, 11526-11530.

Tan, L., Wang, S., Xu, K., Liu, T., Liang, P., Niu, M., Fu, C., Shao, H., Yu, J., Ma, T., *et al.* (2016).

Layered MoS$_2$ Hollow Spheres for Highly-Efficient Photothermal Therapy of Rabbit Liver Orthotopic Transplantation Tumors. Small *12*, 2046-2055.

Tang, W., Dong, Z., Zhang, R., Yi, X., Yang, K., Jin, M., Yuan, C., Xiao, Z., Liu, Z., and Cheng, L. (2019). Multifunctional Two-Dimensional Core–Shell MXene@Gold Nanocomposites for Enhanced Photo–Radio Combined Therapy in the Second Biological Window. ACS Nano *13*, 284-294.

Tian, Q., Jiang, F., Zou, R., Liu, Q., Chen, Z., Zhu, M., Yang, S., Wang, J., Wang, J., and Hu, J. (2011). Hydrophilic Cu$_9$S$_5$ Nanocrystals: A Photothermal Agent with a 25.7% Heat Conversion Efficiency for Photothermal Ablation of Cancer Cells in Vivo. ACS Nano *5*, 9761-9771.

Wan, S.-S., Cheng, Q., Zeng, X., and Zhang, X.-Z. (2019). A Mn(III)-sealed metal-organic framework nanosystem for redox-unlocked tumor theranostics. ACS Nano *13*, 6561-6571.

Wang, D., Shi, R., Zhou, J., Shi, S., Wu, H., Xu, P., Wang, H., Xia, G., Barnhart, T.E., and Cai, W. (2018). Photo-enhanced singlet oxygen generation of Prussian blue-based nanocatalyst for augmented photodynamic therapy. iScience *9*, 14-26.

Wang, Q., Wang, H., Yang, Y., Jin, L., Liu, Y., Wang, Y., Yan, X., Xu, J., Gao, R., Lei, P.*, et al.* (2019a). Plasmonic Pt Superstructures with Boosted Near-Infrared Absorption and Photothermal Conversion Efficiency in the Second Biowindow for Cancer Therapy. Adv. Mater. *31*, 1904836.

Wang, X., Ma, Y., Chen, H., Wu, X., Qian, H., Yang, X., and Zha, Z. (2017). Novel doxorubicin loaded PEGylated cuprous telluride nanocrystals for combined photothermal-chemo cancer treatment. Colloids Surf., B *152*, 449-458.

Wang, X., Zhong, X., Lei, H., Geng, Y., Zhao, Q., Gong, F., Yang, Z., Dong, Z., Liu, Z., and Cheng, L. (2019b). Hollow Cu$_2$Se nanozymes for tumor photothermal-catalytic therapy. Chem. Mater. *31*, 6174-6186.

Wang, X., Zhong, X., Zha, Z., He, G., Miao, Z., Lei, H., Luo, Q., Zhang, R., Liu, Z., and Cheng, L. (2020). Biodegradable CoS$_2$ nanoclusters for photothermal-enhanced chemodynamic therapy. Appl. Mater. Today *18*, 100464.

Yong, Y., Zhou, L., Gu, Z., Yan, L., Tian, G., Zheng, X., Liu, X., Zhang, X., Shi, J., Cong, W.*, et al.* (2014). WS$_2$ nanosheet as a new photosensitizer carrier for combined photodynamic and photothermal therapy of cancer cells. Nanoscale *6*, 10394-10403.